Monthly Notices of the ROYAL ASTRONOMICAL SOCIETY

MNRAS **524,** 5229–5247 (2023) https://doi.org/10.1093/mnras/stad2160
Advance Access publication 2023 July 20

Star formation history of $0.1 \leq z \leq 1.5$ mass-selected galaxies in the ELAIS-N1 Field

E. F. Ocran [1,2]★ M. Vaccari [2,3,4]★ J. M. Stil,[3,5] A. R. Taylor,[2,3] C. H. Ishwara-Chandra[2,6] and Jae-Woo Kim[1]★

[1]*Korea Astronomy and Space Science Institute, 776 Daedeokdae-ro, Daejeon 305-348, Korea*
[2]*Inter-University Institute for Data Intensive Astronomy, Department of Astronomy, University of Cape Town, 7701 Rondebosch, Cape Town, South Africa*
[3]*Inter-University Institute for Data Intensive Astronomy, Department of Physics and Astronomy, University of the Western Cape, 7535 Bellville, Cape Town, South Africa*
[4]*INAF – Istituto di Radioastronomia, via Gobetti 101, I-40129 Bologna, Italy*
[5]*Department of Physics and Astronomy, University of Calgary, 2500 University Drive NW, Calgary AB, T2N 1N4, Canada*
[6]*National Centre for Radio Astrophysics, Tata Institute of Fundamental Research, Pune 411007, India*

Accepted 2023 July 7. Received 2023 July 5; in original form 2023 January 8

ABSTRACT

We measure the specific star formation rates (sSFRs) of *K*-band selected galaxies from the European Large Area ISO Survey North 1 by stacking Giant Metrewave Radio Telescope data at 610 MHz. We identify a sample of star-forming galaxies (SFGs), spanning $0.1 \leq z \leq 1.5$ and $10^{8.5} < M_\star/\mathrm{M}_\odot < 10^{12.4}$, using a combination of multiwavelength diagnostics obtained from the deep LOw Frequency ARray Two-metre Sky Survey multiwavelength catalogue. We measure the flux densities in the radio map and estimate the radio SFR in order to probe the nature of the galaxies below the noise and confusion limits. The massive galaxies in our sample have the lowest sSFRs, which is in agreement with previous studies. For the different populations, we show that the sSFR–mass relation steepens with redshift, with an average slope of $\langle\beta_{\mathrm{All}}\rangle = -0.49 \pm 0.01$ for the whole sample, and $\langle\beta_{\mathrm{SFG}}\rangle = -0.42 \pm 0.02$ for the SFGs. Our results indicate that galaxy populations undergo 'downsizing', whereby most massive galaxies form their stars earlier and more rapidly than low-mass galaxies. Both populations show a strong decrease in their sSFR towards the present epoch. The sSFR evolution with redshift is best described by a power law $(1+z)^n$, where $\langle n_{\mathrm{ALL}}\rangle \sim 4.94 \pm 0.53$ for all galaxies and $\langle n_{\mathrm{SFG}}\rangle \sim 3.51 \pm 0.52$ for SFGs. Comparing our measured sSFRs to results from literature, we find a general agreement in the sSFR–$M_\star$ plane.

Key words: Galaxy: evolution – radio continuum: galaxies.

1 INTRODUCTION

Radio surveys have now reached sufficient areal coverage that they are now dominated by the same galaxies detected by infrared (IR), optical, and X-ray surveys and have become increasingly important in studies of galaxy evolution. The galaxy populations that lie beneath the sensitivity limits of the current deepest surveys have become an important area of study in recent years (see e.g. White et al. 2007; Dunne et al. 2009; Garn & Alexander 2009; Stil et al. 2014; Zwart et al. 2014, and references therein). Deep radio surveys are able to probe the galaxy star formation rate (SFR) due to cosmic ray and synchrotron emission that originate from the accelerated electrons in the magnetic fields of supernova remnants that are the result of massive star formation (Helou, Soifer & Rowan-Robinson 1985).

The relation between SFR and 1.4 GHz luminosity is calibrated to the far-IR–radio correlation (e.g. Condon 1992; Haarsma et al. 2000; Yun, Reddy & Condon 2001; Condon, Cotton & Broderick 2002). At radio wavelengths, observations are not obscured by dust and their higher angular resolution, as compared to IR surveys, significantly reduces source confusion. However, emission from active galactic nuclei (AGNs) represent a significant source of contamination (see Zwart et al. 2014). Ocran et al. (2021) compared the SFR derived from the IR luminosity and the radio power to show that the two are equivalently good tracers of star formation in non-active star-forming galaxies (SFGs) and also for the host galaxies of radio quiet (RQ) AGNs. They studied the correlation between galaxy SFR and stellar mass at different redshifts for SFGs, RQ, and radio loud (RL) AGNs and found that the vast majority of our sources lie on the star formation main sequence (hereafter, MS) when using IR SFRs.

The MS of SFGs is a fundamental relation in galaxy evolution that relates galaxy star formation to their stellar mass (see Elbaz et al. 2007; Noeske et al. 2007; Pannella et al. 2009; Oliver et al. 2010; Reddy et al. 2012; Whitaker et al. 2012, 2014; Popesso et al. 2019a,b; Leslie et al. 2020). However, in the literature there is no common agreement on the form of the MS. There is contention whether the MS is linear across all redshifts (see Wuyts et al. 2011a,b; Speagle et al. 2014; Schreiber et al. 2015; Pearson et al. 2018), or has a flattening or turnover at stellar masses $\log_{10}(M_\star/\mathrm{M}_\odot) > 10.5$ (see Whitaker et al. 2014; Lee et al. 2015; Leslie et al. 2020; Thorne et al. 2021). The specific SFR (sSFR; SFR divided by stellar mass)

★ E-mail: ocran62@gmail.com (EO); mattia.vaccari@gmail.com (MV); kjw0704@kasi.re.kr (JK)

© 2023 The Author(s).
Published by Oxford University Press on behalf of Royal Astronomical Society. This is an Open Access article distributed under the terms of the Creative Commons Attribution License (http://creativecommons.org/licenses/by/4.0/), which permits unrestricted reuse, distribution, and reproduction in any medium, provided the original work is properly cited.

Downloaded from https://academic.oup.com/mnras/article/524/4/5229/7227354 by Western Cape University user on 25 April 2024

provides a measure of the current star formation activity related to the past history (Sandles et al. 2022). Studies have shown that the galaxy stellar mass function (SMF) at high masses evolves fairly slowly up to $z \sim 0.9$, and then more rapidly up to at least $z \sim 2.5$, suggesting that the majority of stellar mass assembly took place at $z \gtrsim 1$ (see Feulner et al. 2007; Pozzetti et al. 2007). At low masses, Cassata et al. (2007) showed that the mass of a galaxy plays an important role in star formation, at $z \lesssim 1$. However, at $z \lesssim 0.2$, ongoing star formation in massive galaxies is almost entirely absent (see Thorne et al. 2021). The evolution of the slope sSFR–$M_\star$ plane as a function of redshift, on mass-dependent time-scales, has been found to decline significantly but smoothly (see Speagle et al. 2014). Moreover, the sSFR plateaus at higher redshifts, $z \gtrsim 3$, and continues to increase with a relatively shallow slope as noted in Behroozi, Wechsler & Conroy (2013). Studies like Davidzon et al. (2018) have used the differential evolution of the galaxy SMF to infer the sSFR evolution of galaxies.

The sensitivities achieved by SKA pathfinders and eventually the SKA itself will have a huge impact on our understanding of star formation in galaxies and its co-evolution with supermassive black holes (Padovani 2011). Improvements in both depth and sky coverage are being made with these surveys, with narrow, but very deep surveys such as the MeerKAT MIGHTEE (Jarvis et al. 2016) and wide-area radio data such as Evolutionary Map of the Universe (EMU; Norris 2011). These new surveys are probing unexplored volume of the Universe. Studies have shown that at the faintest radio flux densities ($S_{1.4} < 10$ mJy), conflicting results emerge regarding whether there is a flattening of the average spectral index between a low radio frequency (325 or 610 MHz) (see Randall et al. 2012). More comprehensive observations of the shape of the radio spectrum, extending to lower frequencies, will ensure a maximum scientific return by combining the deep radio continuum data at GHz frequencies.

Stacking is a common tool that has been used to investigate the star formation properties of galaxies at far greater sensitivity by combining many observations of individual galaxies at the expense of any specific knowledge of the individual galaxies that make up the stack. For example, Dunne et al. (2009) used stacking of 610 MHz and 1.4 GHz data from the VLA and the Giant Metrewave Radio Telescope (GMRT) to investigate the star formation history of *BzK*-selected galaxies from the UKIRT Infrared Deep Sky Survey (UKIDSS–UDS) and computed stellar masses using the absolute *K*-band magnitude. Karim et al. (2011) calculated stellar masses using spectral energy distribution (SED) fitting from their photometric-redshift fitting by selecting galaxies at 3.6 μm, and stacked 1.4 GHz VLA data (A and C arrays), with a noise of 8 μJy at the centre of their 1.72 deg^2 map. They found a good agreement in their radio-derived sSFR–redshift evolution between their studies and that of Dunne et al. (2009), however, the dependence of sSFR on stellar mass was found to be much shallower for the UKIDSS data than for COSMOS. Zwart et al. (2014) stacked deep (17.5 μJy) VLA radio observations at the positions of K_s-selected sources in the VIDEO field for $K_s < 23.5$ and sensitive to $0 < z \lesssim 5$. They found that sSFR falls with stellar mass, in agreement with the 'downsizing' paradigm. Leslie et al. (2020) measured the MS using mean stacks of 3 GHz radio continuum images to derive average SFRs for ∼200 000 mass-selected galaxies at $z > 0.3$ in the COSMOS field. They described the MS by adopting a new model that incorporates a linear relation at low stellar mass ($\log(M_\star/\mathrm{M}_\odot) < 10$) and a flattening at high stellar mass that becomes more prominent at low redshift (i.e. $z < 1.5$).

We present an independent stacking analysis of radio data from the GMRT surveys of the European Large Area ISO Survey North 1 (ELAIS-N1) region. We stack by mass and redshift bins, respectively, for sources drawn from the rich LOw Frequency ARray (LOFAR) Two-metre Sky Survey (LoTSS; Shimwell et al. 2017) deep field multiwavelength ancillary data available in the field. We calibrate 610 MHz rest-frame luminosity as an SFR indicator following Garn et al. (2009), allowing us to turn radio luminosity estimates into SFR function estimates. We provide a coherent, uniform measurement of the evolution of the logarithmic sSFR–stellar mass ($M_\star$) relation, for star-forming and all galaxies out to $z \sim 1.5$. Using median stacked images at 610 MHz, we derive average SFRs and sSFRs for ∼ 77 047 mass-selected galaxies, spanning $0.1 \leq z \leq 1.5$ and $10^{8.5} < M_\star/\mathrm{M}_\odot < 10^{12.4}$ in the ELAIS-N1. We aim to answer how the sSFRs change as a function of stellar mass and redshift with regards to a deep 610 MHz low-frequency continuum survey, which are complimentary to sSFRs derived at the high frequency observations.

The paper is arranged as follows: The data sets used in this work are described in Section 2. In Section 3, we describe the prescription we used in selecting the sample for our analyses. Section 4 presents the analyses and results from our stacking experiment. We compare the synergies between our work and findings from the literature in Section 5.1. We then provide our discussions and a summary of our work in Sections 5 and 6, respectively. We assume a flat cold dark matter (ΛCDM) cosmology with $\Omega_\Lambda = 0.7$, $\Omega_\mathrm{m} = 0.3$, $H_\mathrm{o} = 70\ \mathrm{km\,s^{-1}\,Mpc^{-1}}$, and $S_\nu \propto \nu^\alpha$ for calculation of intrinsic source properties.

2 DATA SETS

In this section, we discuss the different data sets we use for our investigation. These data are all taken from publicly available catalogues.

2.1 Radio data sets

We employ the 610 MHz wide-area survey (Ishwara-Chandra et al. 2020) of the ELAIS-N1 region (Oliver et al. 2000), using the GMRT. These data are in hexagonal configuration centred on $\alpha = 16^\mathrm{h}\ 10^\mathrm{m}\ 30^\mathrm{s}, \delta = 54^\circ\ 35\ 00''$. The 610 MHz wide-area survey consists of 51 pointings, mosaicked to create an image of ELAIS-N1 covering ∼ 12.8 deg^2. The full width at half-maximum (FWHM) of the synthesized beam varies between 4.5 and 6 arcsec. Before mosaicking, the image from each field was smoothed to a circular Gaussian beam with FWHM of 6 arcsec. The final rms in the total intensity mosaic image is ∼ 40 μJy beam^{-1}. Ishwara-Chandra et al. (2020) indicated that this is equivalent to ∼ 20 μJy beam^{-1} rms noise at 1.4 GHz for a spectral index of −0.75, which is several times deeper than the VLA FIRST survey at similar resolution. The resulting mosaic is about 3.6 × 3.6 deg^2 (see Ishwara-Chandra et al. 2020). The criterion Ishwara-Chandra et al. (2020) used to distinguish point sources from resolved sources resulted in about 60 per cent of sources being unresolved by using $S_\mathrm{total}/S_\mathrm{peak} < 1$ (see Prandoni et al. 2001), and an extra term to fit the envelope. By considering a total to peak flux ratio <1.5, ∼75 per cent of sources were found to be unresolved.

2.2 The LOFAR science-ready multiwavelength catalogue of the ELAIS-N1

The LOFAR (van Haarlem et al. 2013) LoTSS deep field multiwavelength data we use are only briefly described here, for much greater detail, the reader is referred to Shimwell et al. (2017, 2019, 2022), Kondapally et al. (2021), and subsequent data release papers. LoTSS

Downloaded from https://academic.oup.com/mnras/article/524/4/5229/7227354 by Western Cape University user on 25 April 2024

is an ongoing sensitive, high-resolution 120–168 MHz survey of the entire northern sky for which the first full-quality public data release covers 424 square degrees with a median rms noise of 71 μJy at 150 MHz (Sabater et al. 2019; Williams et al. 2019). The second data release covers 27 per cent (i.e. split into two regions spanning 4178 and 1457 square degrees) of the northern sky with a central frequency of 144 MHz down to a median rms sensitivity of 83 μJy beam^{-1} (see Shimwell et al. 2022). The ELAIS-N1 field is the deepest of the LoTSS deep fields to date and one of the areas that has the most extensive ancillary data (Sabater et al. 2021).

The LOFAR team has provided science-ready multiwavelength data in three fields along with the full complimentary optical/IR catalogue presented by Kondapally et al. (2021). The photometric redshift estimates for all plausible counterparts were produced from a complete, homogeneous sample of objects measured across optical to IR wavelength. This is achieved by building a forced, matched aperture, multiwavelength catalogue in each field spanning the ultraviolet (UV) to mid-IR wavelengths using the latest deep data sets. The full details of the photo-z estimation, are presented in a companion release paper (see Duncan et al. 2021, for more details).

2.3 Stellar masses

Galaxy stellar masses were obtained from science-ready multiwavelength catalogue (see Duncan et al. 2021, for more details). This is the total stellar mass of a galaxy in units of solar mass and was estimated using the PYTHON-based SED fitting code previously used by Duncan et al. (2014, 2019). Stellar population synthesis models of Bruzual & Charlot (2003) for a Chabrier (2003) initial mass function (IMF) were generated for composite stellar population models with three different stellar metallicities of $Z_\odot = 0.1, 0.4, 1.0$. Duncan et al. (2021) used a grid of star formation histories based on the double power-law model with the priors on the range of power-law slopes and turnover ages taken from Carnall et al. (2019). They argued this provides sufficient flexibility to accurately describe the star formation histories of a wide range of possible formation and quenching mechanisms. A simple prescription for nebular emission is included in the model SEDs. Further details of the assumed emission-line ratios for Balmer and metal lines, as well as the nebular continuum prescription, can be found in Duncan et al. (2014). They also incorporate dust attenuation following the two-component dust model of Charlot & Fall (2000). The ELAIS-N1 field is complete to significantly lower masses when using K band to select samples at $z < 1$, where deeper near-IR observations are provided by UKIDSS Deep Extragalactic Survey (DXS; Lawrence et al. 2007). From simple estimations of the galaxy SMFs within the ELAIS-N1 field and comparison with the literature, Duncan et al. (2021) validated that the stellar masses provide reliable and self-consistent estimates suitable for statistical studies across the whole field.

Following Duncan et al. (2021), we empirically estimate the stellar mass completeness (Pozzetti et al. 2010; Davidzon et al. 2013, 2017; Ilbert et al. 2013; Laigle et al. 2016). This is determined by the 3σ magnitude limit, $K_{\rm lim} = 22.7$ mag. In Fig. 1, we show the distribution of stellar mass ($M_\star$) with the redshift (z) for the galaxies in the ELAIS-N1 field. For each redshift bin, we estimate the stellar mass completeness $M_{\rm lim}$ within which 90 per cent of the galaxies lie. The measured stellar masses for the sample are scaled to the magnitude limit: $\log_{10} M_{\rm lim} = \log_{10} M - 0.4(K_{\rm lim} - K)$ and the mass completeness limit derived from 95th percentile of the scaled $M_{\rm lim}$ mass distribution. The black circles in Fig. 1 represent the mass limit in each redshift bin and the solid green curve represents the fit to $M_{\rm lim}$ the mass limit. Table 1 presents the calculated mass limits for each redshift bin in this study of ELAIS-N1 LoTSS deep field for the full sample. Our sources should be largely complete above the cuts. The distributions are generally consistent among different fields, supporting the self-consistency of our results.

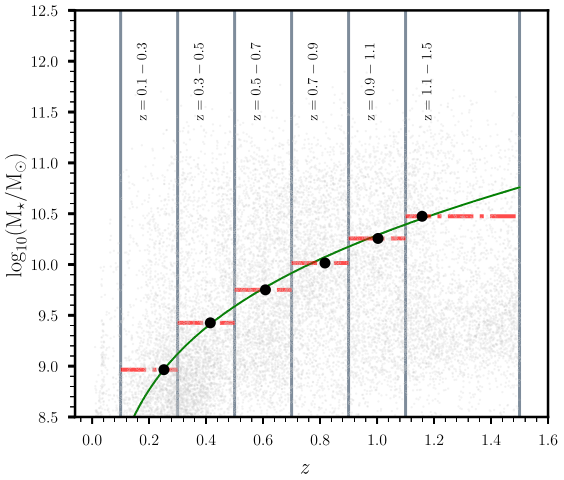

Figure 1. Observed stellar mass distribution as a function of redshift for the ELAIS-N1 LoTSS deep field. The background density plot shows the mass distribution of sources with the solid black circles showing the 90 per cent mass completeness limit of the K reference band in the ELAIS-N1 field derived empirically (see Pozzetti et al. 2010) at the median redshift in each bin. Here, we a plotting ∼80 per cent of the data points. The solid green curve represents the fit to $M_{\rm lim}$, the mass limit.

Table 1. Mass limits for each redshift bin in this study of ELAIS-N1 LoTSS deep field for the full sample.

Bin	$M_{\rm lim}^{\rm full}$
0.1−0.3	8.96
0.3−0.5	9.42
0.5−0.7	9.75
0.7−0.9	10.01
0.9−1.1	10.25
1.1−1.5	10.47

3 SAMPLE SELECTION

In this section, we describe the sample and the multiwavelength diagnostics employed to obtain a census of galaxies showing evidence of hosting an AGN within this sample.

Previous studies of the sSFR–$M_\star$ plane indicate that galaxies reside in two populations. The first is the SFG population whose SFR is positively correlated with stellar mass out to redshifts, $z \sim 4$ (see Karim et al. 2011; Schreiber et al. 2015; Tomczak et al. 2016; Leslie et al. 2020). The second population consists of quiescent galaxies (QGs) that are not actively forming stars and typically reside at the high-mass end (i.e. they have lower sSFR; Renzini & Peng 2015). In this section, we describe how we separate QGs, which are systems with little or no ongoing star formation and large surface stellar mass density, from SFGs (see Patel et al. 2011, 2012). This method is most efficient in excluding QGs (see Leja et al. 2019a; Leja, Tacchella & Conroy 2019b). These QGs have very low SFR by definition, and they are preferentially found at high $M_\star$ (see Schreiber et al. 2015).

The sources classified as SFGs are those sources in our redshift and mass-selected bins satisfy the colour cuts in the diagnostics employed in this study.

Downloaded from https://academic.oup.com/mnras/article/524/4/5229/7227354 by Western Cape University user on 25 April 2024

3.1 The sample

Extensive details of the photometric redshift and stellar mass (limited to $z < 1.5$) estimation included in the LOFAR science-ready multi-wavelength data are outlined in Duncan et al. (2021). We followed the prescription by Jarvis et al. (2013) in order to remove sources that could be spectroscopically and photometrically flagged as stars. This star galaxy separation criterion clearly segregates the two types of objects in rest-frame $J - K$ versus $u - J$ colour space. We found that galaxies dominate the catalogue at $K > 22.7$ mag.

We then applied the prescription below to select our sample:

$$\left(\frac{z_{1,\max} - z_{1,\min}}{1 + z_{1,\text{median}}}\right) \times 0.5 < 0.1 \,\&\, \left(\frac{S_K}{S_{\text{Kerr}}}\right) > 5 \,\&\, (z_{\text{best}} \leq 1.5) \,\&\, (10^{8.5} < M_\star/M_\odot < 10^{12.4}), \quad (1)$$

where the best available estimate is z_{best}, including spectroscopic redshifts when available and photometric redshift (photo-z) estimates otherwise. $z_{1,\text{median}}$ is the primary redshift peak used when calculating the photo-z. Whereas $z_{1,\min}$ and $z_{1,\max}$ are the lower and upper bounds of the primary 80 per cent highest probability density (HPD) credible interval (CI) peak, respectively. The S_K and S_{Kerr} represent the near-IR UKIDSS Deep Extragalactic Survey (DXS; hereafter UKIDSS-DXS) DR10 K-band flux and flux error, respectively. These near-IR data cover a maximum area of around 8 deg^2 with a 3σ and 5σ magnitude depths of 22.7 and 22.1 mag respectively, in ELAIS-N1. Following equation (1), we select ∼77 047 sources that constitute our sample. Further selection cuts (i.e. SFG/AGN /QG separation) applied to the sample are described in subsequent sections.

3.2 AGN removal using IRAC colour diagnostics

AGNs are known to show flux variability over all observable timescales and across the entire electromagnetic spectrum hence a combination of multiwavelength diagnostics are usually employed (see Villarroel & Korn 2014).

Cochrane et al. (2023) used reliable classifications of SFGs from Best et al. (2023) to study the cosmic star formation history in the Elais-N1, covering over 90 per cent of cosmic time (i.e. $0 \leq z \leq 4$). We applied the original AGN flag given in the LoTSS multiwavelength catalogue (from Best et al. 2023) in order to remove galaxies showing evidence of hosting an AGN. This AGN flag in the catalogue incorporates:

(i) optAGN: Sources included in the Million Quasar Catalogue compilation or spectroscopically identified AGNs.

(ii) IRAGN: When a source satisfies Donley et al. (2012) IR AGN criterion given by

$$x = \log_{10}\left(\frac{f_{5.8\mu\text{m}}}{f_{3.6\mu\text{m}}}\right), \quad y = \log_{10}\left(\frac{f_{8.0\mu\text{m}}}{f_{4.5\mu\text{m}}}\right) \quad (2)$$

$$x \geq 0.08 \wedge y \geq 0.15$$
$$\wedge y \geq (1.21 \times x) - 0.27$$
$$\wedge y \leq (1.21 \times x) + 0.27$$
$$\wedge f_{4.5\mu\text{m}} > f_{3.6\mu\text{m}} > f_{4.5\mu\text{m}} \wedge f_{8.0\mu\text{m}} > f_{5.8\mu\text{m}}. \quad (3)$$

(iii) XrayAGN: When a source has X-ray counterpart.

Following the *optAGN*, *IRAGN*, and *XrayAGN* flags, we select 428 sources satisfying equation (1) as candidate AGN. It is important to note that every technique for selecting AGN is affected by selection biases, and these ones are no exception. The colour selection means that objects whose observed mid-IR colours are not dominated by thermal emission from AGN will be missing from the sample. Fig. 2 presents IRAC colour–colour diagram showing the separation between AGNs (red scatter contour) and SFGs (blue scatter contour). For comparison, we show the Donley et al. (2012) colour selection criterion given by equation (3), and represented by the solid black wedge in the left-hand panel. The solid grey and dotted dashed grey lines indicate the Lacy et al. (2004) and Lacy et al. (2007) wedges, respectively. We also compare the AGN selection based on the Stern et al. (2005) IRAC [3.6]–[4.5] versus [5.8]–[8.0] in Vega magnitudes shown in the right-hand panel of Fig. 2.

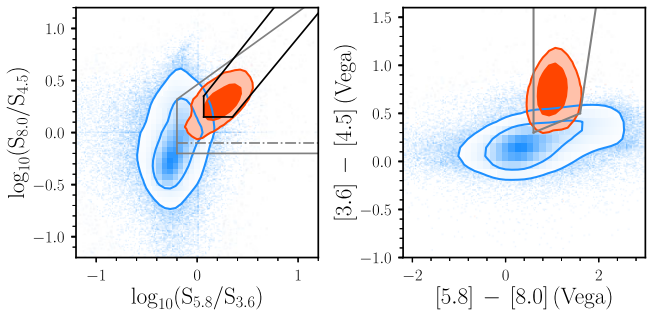

Figure 2. IRAC colour–colour diagram showing the separation between AGNs (red scatter contour) and SFGs (blue scatter contour). The solid black wedge in the left-hand panel indicates the Donley et al. (2012) wedge. Also shown are solid grey lines in the left-hand and right-hand panels indicating colour selection wedges of the Lacy et al. (2004) and Stern et al. (2005), respectively. The dotted dashed grey line in the left-hand panel indicate the Lacy et al. (2007) wedge.

3.3 SFG/quiescent galaxy separation

We aim to create well-defined, unbiased samples of the SFG population. Following Schawinski et al. (2014), one can separate red, green valley, and blue cloud populations using the dust-corrected colour–mass diagram for all redshift bins using: $u - r(M_\star) = -0.24 + 0.25 \times M_\star$ and $u - r(M_\star) = -0.75 + 0.25 \times M_\star$. Fig. 3 presents the $u - r$ colour–stellar mass dust-corrected diagram for our sample. Galaxies with 'green' or intermediate colours are those galaxies in which star formation is in the process of turning off, but still have some ongoing star formation – indicating the process only shut down a short while ago, ∼ 10^8 yr (Bell et al. 2004). The 'green valley' region represents the crossroads of galaxy evolution. Galaxies that constitute this population are between the blue SFGs (the 'blue cloud') and the red, passively evolving galaxies (the 'red sequence'). The colour bimodality is weakly evident in the redshift bins at 0.1–0.3 and 0.3–0.5 of the rest-frame $u - r$ colour distribution. Subsequent redshift bins exhibit a unimodal distribution peaking in the blue (these are the main-sequence SFGs). In particular, the colour–mass or colour–magnitude diagrams do not exhibit strong colour bimodality seen in of the *UVJ* or *NUVrJ* diagrams (see Williams et al. 2009; Muzzin et al. 2013; Straatman et al. 2014, 2016).

Similarly, observational results have also been presented by Borch et al. (2006) and Brammer et al. (2009) who used the $U - V$ colour–mass relation to separate red galaxies from blue galaxies at $0.2 \leq z \leq 1.0$ and $0. \leq z \leq 2.5$, respectively. Peng et al. (2010) used the $U - B$ with redshift evolution extrapolated to $z = 1$ to split into red and blue galaxies. More recently, Powell et al. (2017) used the rest-frame $U - R$ colour $0.7 \leq z \leq 1.3$ to distinguish between red and blue sequence galaxies.

Downloaded from https://academic.oup.com/mnras/article/524/4/5229/7227354 by Western Cape University user on 25 April 2024

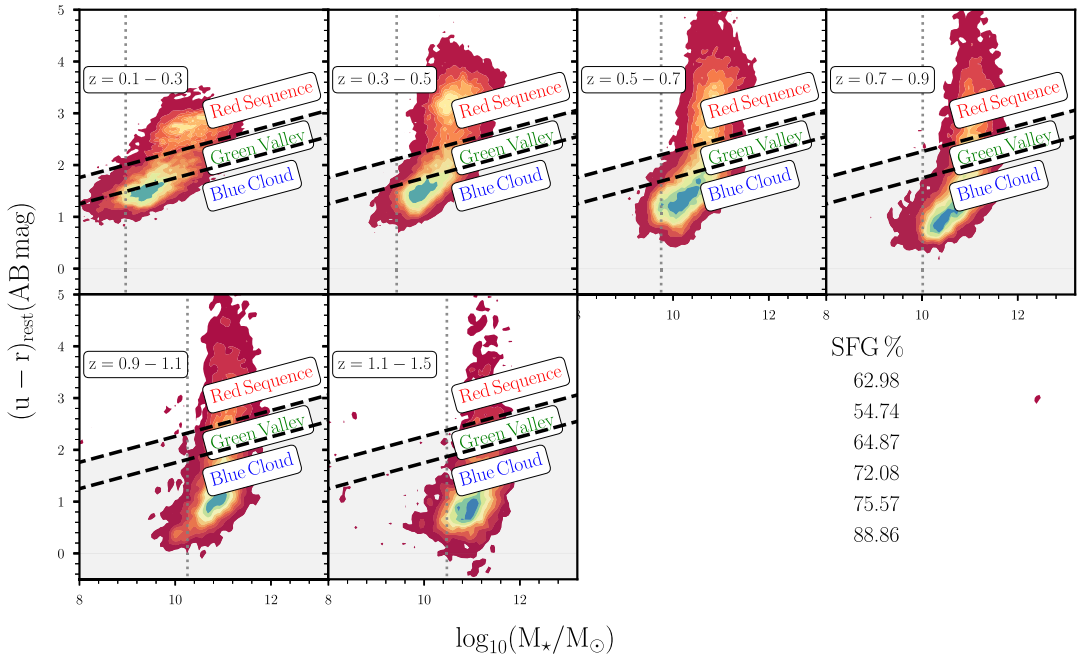

Figure 3. The $u - r$ galaxy colour–mass diagram in bins of redshift as density contours. The galaxy colour–mass diagram showing blue, SFGs are at the bottom, in the blue cloud region. The red, quiescent/passively evolving galaxies are at the top, in the red sequence. The 'green valley' is the transition zone in between. The dotted vertical lines indicate mass completeness limits for each redshift bin.

For simplicity, we consider only two states for galaxies, 'blue star-forming' and 'red passive' based on a dividing rest-frame $u - r$ colour. Obviously, this approach is partly simplistic, but is in accordance with our approach to identify the most basic features of the SFG population. Since the V and r bands are not equivalent, we therefore adhere to using only the Schawinski et al. (2014), $u - r(M_\star) = -0.24 + 0.25 \times M_\star$ line to separate red, quiescent/passively evolving galaxies from blue star-forming (i.e. potentially including green valley) ones. Thus, the grey shaded area in each panel of Fig. 3 represents the region in which we classify a source as an SFG. We indicate the corresponding percentage of SFGs (i.e. green and blue galaxies) for each redshift bin in Fig. 3 from the first to the last redshift bin. Appendix A provides more discussions on our colour–mass selection.

Following the AGN diagnostics in Section 3.2, and the separation of quiescent/passively evolving galaxies from candidate SFGs, we employ our final sample selected for the subsequent analyses as follows:

(1) All galaxies: The original 77 047 sources that satisfying equation (1).

(2) SFGs: Sources from the original 77 047 sample that are classified as SFGs based on the $u - r$ galaxy colour–mass diagnostics and sources that are not labelled as *optAGN*, *IRAGN*, and *XrayAGN* from the LoTSS multiwavelength catalogue. Removing these flags, we obtain a subsample of 51 124 as SFGs.

Table 2 presents a summary of the results of subsequent analysis of the average galaxy mass in each stellar mass range. For a given stellar mass range, we show the median stellar across the entire redshift range (i.e. $0.1 \leq z \leq 1.5$) of this work, for the corresponding total and SFG populations. The lower and upper bounds represent the 16/84th percentile.

Table 2. Table showing the summary of the results of subsequent analysis of the average galaxy properties in each stellar mass range.

M range	$N_{\rm All\ galaxies}$	$\left(\log \frac{M_\star}{M_\odot}\right)_{\rm ALL\ GALAXIES}$	$N_{\rm SFGs}$	$\left(\log \frac{M_\star}{M_\odot}\right)_{\rm SFGs}$
$8.5 < M_\star < 9.0$	1393	$8.86^{+0.12}_{-0.18}$	1314	$8.84^{+0.15}_{-0.18}$
$9.0 < M_\star < 9.5$	4919	$9.37^{+0.10}_{-0.19}$	4522	$9.36^{+0.11}_{-0.20}$
$9.5 < M_\star < 10.0$	12 853	$9.84^{+0.13}_{-0.17}$	10 812	$9.82^{+0.13}_{-0.17}$
$10.0 < M_\star < 10.5$	20 580	$10.30^{+0.12}_{-0.17}$	14 343	$10.28^{+0.12}_{-0.17}$
$10.5 < M_\star < 11.0$	24 766	$10.76^{+0.12}_{-0.16}$	13 805	$10.74^{+0.12}_{-0.17}$
$11.0 < M_\star < 12.4$	12 536	$11.16^{+0.24}_{-0.17}$	6328	$11.15^{+0.23}_{-0.17}$

4 ANALYSIS AND RESULTS

4.1 Stacking methodology

The direct detection of the radio point source population is complicated by source confusion. Confusion is the blending of faint sources within a telescope beam. Hence statistical techniques such as stacking, which are not strongly effected by confusion noise, can be a powerful tool for reaching below the noise. Stacking is a tool to average together data for a given set of objects. For an input sample of N galaxies, its background noise level in a stacked image should reduce to $\sim 1/\sqrt{\rm N}$ of the noise measured in a single radio image. Stacking is at the expense of knowledge of the individual galaxies, but with careful application of criteria when binning the galaxies, and with a large enough sample, it can reveal properties of galaxies below the noise and confusion levels. The technique has been used to great effect many times in the literature (see Serjeant et al. 2004; Ivison et al. 2007; Bourne et al. 2011, for example).

We choose six bins with a stellar mass and redshift range of $10^{8.5} < M_\star/{\rm M}_\odot < 10^{12.4}$ and $0.1 \leq z \leq 1.5$, respectively. Out of the 77 047 sources we select as all galaxies, 51 124 sources are SFGs. We stack the K-band mass-selected positions from the LOFAR multiwavelength catalogue of the ELAIS-N1 on the 610 MHz wide

Downloaded from https://academic.oup.com/mnras/article/524/4/5229/7227354 by Western Cape University user on 25 April 2024

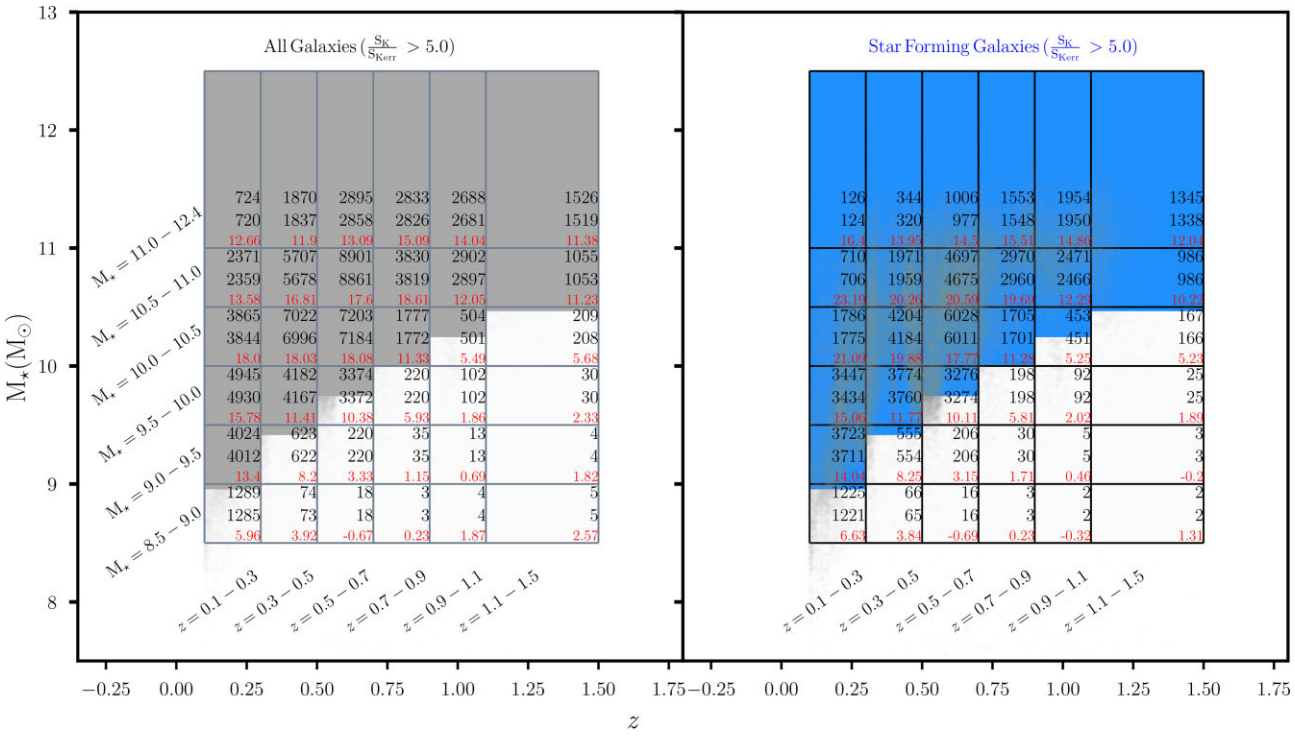

Figure 4. Binning scheme in stellar mass and photometric redshift for the entire (left) and the SF (right) sample. The top number in each box is the total number of galaxies in each bin. The middle number is the total number of galaxies used in the median radio stack; the bottom number shows the SNR achieved in the median radio stack. The grey and blue shading traces the mass completeness limits derived for all galaxies in Section 2.3 (see Table 1).

radio map (Ishwara-Chandra et al. 2020) of the ELAIS-N1. Stacking was done with the Python Astronomical Stacking Tool Array (PASTA; Keller & Stil 2018) program,[1] which measures the flux in a map from selected sources (usually at another wavelength) and then builds a distribution of map-extracted fluxes for the sample (White et al. 2007). We choose fixed bin sizes and non-overlapping (statistically independent) bins in stellar mass and redshift space. This allows for a statistically robust number of sources of in each bin and allows us to achieve a high signal-to-noise ratio (SNR). Notice that there is a ∼0.5 dex in mass, i.e. $M_\star$ bin size, up to $M_\star(M_\odot) = 11.0$, beyond which the bin size is increased to ∼1.4 dex in order to cover the full mass range. Conversely, there is a ∼0.25 dex redshift bin size over the entire redshift range. The advantage of stacking technique is the gain in the SNR, as combining many sources reduces the random noise while maintaining the average level of the signal. Median stacking analyses are less susceptible to contamination from radio AGNs, which constitute a minority of the population at faint radio fluxes as compared to mean stacking (Smolčić et al. 2017; Algera et al. 2020).

Our stacking work is summarized as follows:

(i) An input list of coordinates is created for the number of galaxies to be stacked, taking into consideration the selection criteria. An input image in FITS format.

(ii) PASTA reads the source list and FITS file with the number of pixels specified (i.e. 30 × 30 pixels cutouts for our 610 MHz image). The program proceeds to extract 'stamps', square sections of the source image with a source centred within them and generating two-dimensional matrices of the median and mean output images. The detection threshold is improved by stacking images centred on the object coordinates.

(iii) The integrated and peak flux densities are computed by running PYBDSF source finder (Mohan & Rafferty 2015) on the median stacked images. PYBDSF fits a 2D Gaussian to any significant emission in the centre of the stack.

The median estimator is more robust to outliers than the mean, and we will demonstrate that the median is the most appropriate choice for our analysis. The median image provides a compelling visual impression of the statistical significance of the sample median compared to nearby off positions. The premise of median stacking a survey is that the radio emission is unresolved, and that the central pixel represents the flux density of the sources in the stack. White et al. (2007) performed detailed calculations that show that a median stacking analysis is superior to a mean stacking, since it is robust to small numbers of bright sources, and it does not require any maximum allowed flux density cut-off prior to stacking. It also shows patterns like the side lobes of the dirty beam that must be present around real sources of any flux density in the image.

Fig. 4 shows the binning scheme in stellar mass and photometric redshift for the entire (left) and the SF (right) sample. The top number in each box is the total number of galaxies in each bin. The middle number is the total number of galaxies used in the radio stack; the bottom number shows the SNR achieved in the radio stack. Ideally, one could roughly estimate stellar mass completeness limits by visual inspection of Fig. 4. Fig. 5 presents the stacked images of total intensity for all galaxies. The columns indicate the median stacked 610 MHz total intensity radio images for total galaxies within the range $z \in [0.1 - 0.3]$, $[0.3 - 0.5]$, $[0.5 - 0.7]$, $[0.7 - 0.9]$, $[0.9 - 1.1]$, and $[1.1 - 1.5]$ for the K-band magnitude mass-selected sample. The rows indicate mass range,

[1] https://github.com/bwkeller/PASTA

Downloaded from https://academic.oup.com/mnras/article/524/4/5229/7227354 by Western Cape University user on 25 April 2024

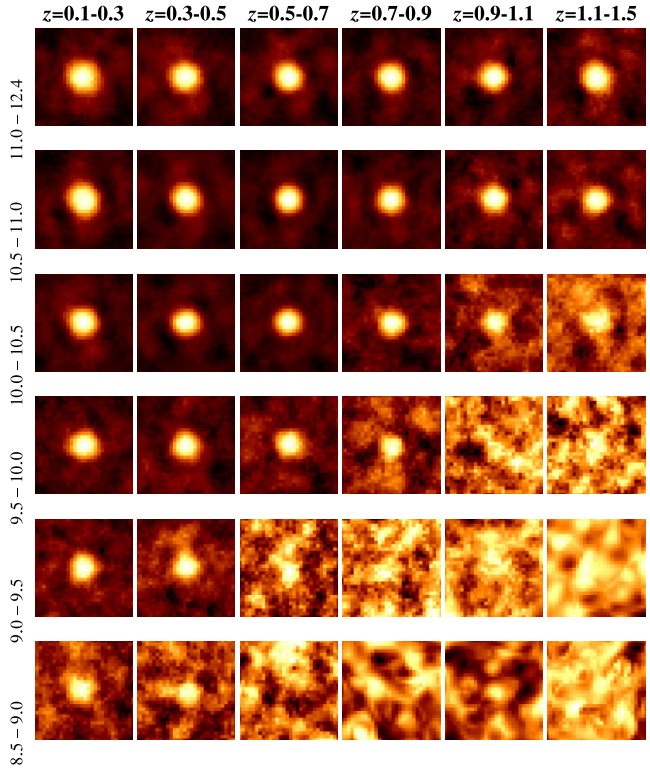

Figure 5. Stacked images (GMRT, 610 MHz) of total intensity for all galaxies. The columns indicate the median stacked 610 MHz total intensity radio images for total galaxies within the range $z \in [0.1-0.3]$, $[0.3-0.5]$, $[0.5-0.7]$, $[0.7-0.9]$, $[0.9-1.1]$, and $[1.1-1.5]$ for the K-band magnitude mass-selected sample. All images have a size of $\sim 36 \times 36$ arcsec^2. The rows indicate mass range, $M_\star \in [11.0-12.4]$, $[10.5-11.0]$, $[10.0-10.5]$, $[9.5-10.0]$, $[9.0-9.5]$, and$[8.5-9.0]$ respectively, from top to bottom. All image-scale ranges between 1 and 100 μJy beam^{-1}.

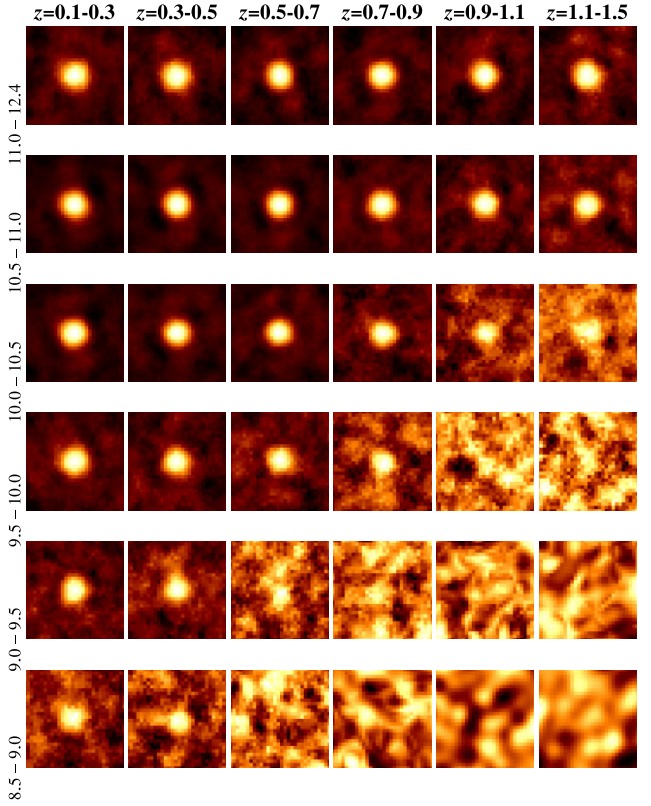

Figure 6. Stacked images (GMRT, 610 MHz) of total intensity for SFGs. The empty space in the last column (i.e. $z \in [1.1–1.5]$) represents redshift range where no median stacked 610 MHz image was produced for the selected SFG population. See Fig. 5 for more details.

$M_\star \in [11.0-12.4]$, $[10.5-11.0]$, $[10.0-10.5]$, $[9.5-10.0]$, $[9.0-9.5]$, and $[8.5-9.0]$, respectively, from top to bottom. All images have a size of $\sim 36 \times 36$ arcsec^2, respectively. The image-scale ranges between 1 and 100 μJy beam^{-1}. The stacked images (GMRT, 610 MHz) of total intensity for SFGs are shown in Fig. 6. In contrast to this, Fig. 7 shows the mean stacked images for the same redshift and stellar mass bins for the total (top) and the SFG (bottom) populations, respectively. All images are notably noisier than their median equivalents, and bright sources away from the centre of the cut-out images have a much greater effect on the stacked images. Thus, the mean images are strongly biased by a few bright radio sources and as such not a good representation of the typical sources within each flux density bin with the noise level of the mean stacked images generally ∼1.5 times the noise of the median stacked images.

Fig. 8 shows the stacked median axial ratio (angular size) $B_{\rm maj}/B_{\rm min}$ as a function of median redshift for all galaxies (left) and SFGs (right). The errors represent the difference between the maximum Gaussian fit to a source and best-fitting Gaussian that encompasses the full source at the centre of the median stacked image. The fitted angular size is overall closely consistent with the original beam size of the 610 MHz image. At the first redshift range for SFGs (i.e. $z \in$ [0.1–0.3]), the size of the Gaussian fits to the median stacked image with $M_\star \in [11.0–12.4]$, seem higher than the size of the synthesized beam $B_{\rm maj}/B_{\rm min} = 1$ (see the horizontal solid green line in Fig. 8). The rest of the mass bins are consistent with the beam when compared with the horizontal solid green line. Differences may occur

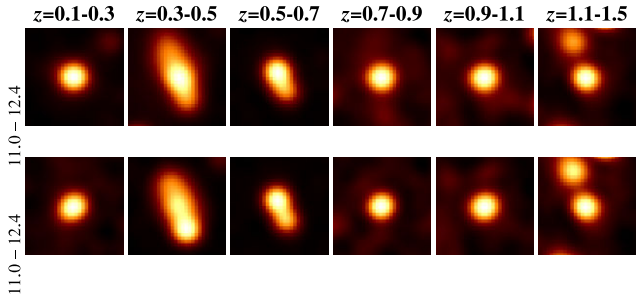

Figure 7. Mean stacked 610 MHz radio images for the same redshift and stellar mass bins for all galaxies (top) and the SFG (bottom) populations, respectively. See Fig. 5 for more details.

for various reasons, for example, a Gaussian fit to a source convolved with a non-Gaussian point spread function can give rise to systematic errors. Errors in the positions of the input source catalogue can lead to blurring of the stacked image. The same effect can occur if the radio emission is systematically offset from the IR emission, in some cases. Fitting of source sizes is a simple test one can run on the results of a stack. This can be used as a test of both the positional accuracy, and in testing that the sources stacked are indeed unresolved. Since our stacked image produces a source that is almost the same size of the beam, this confirms that the positional accuracy is sufficient, and that the stack is dominated by unresolved sources.

Downloaded from https://academic.oup.com/mnras/article/524/4/5229/7227354 by Western Cape University user on 25 April 2024

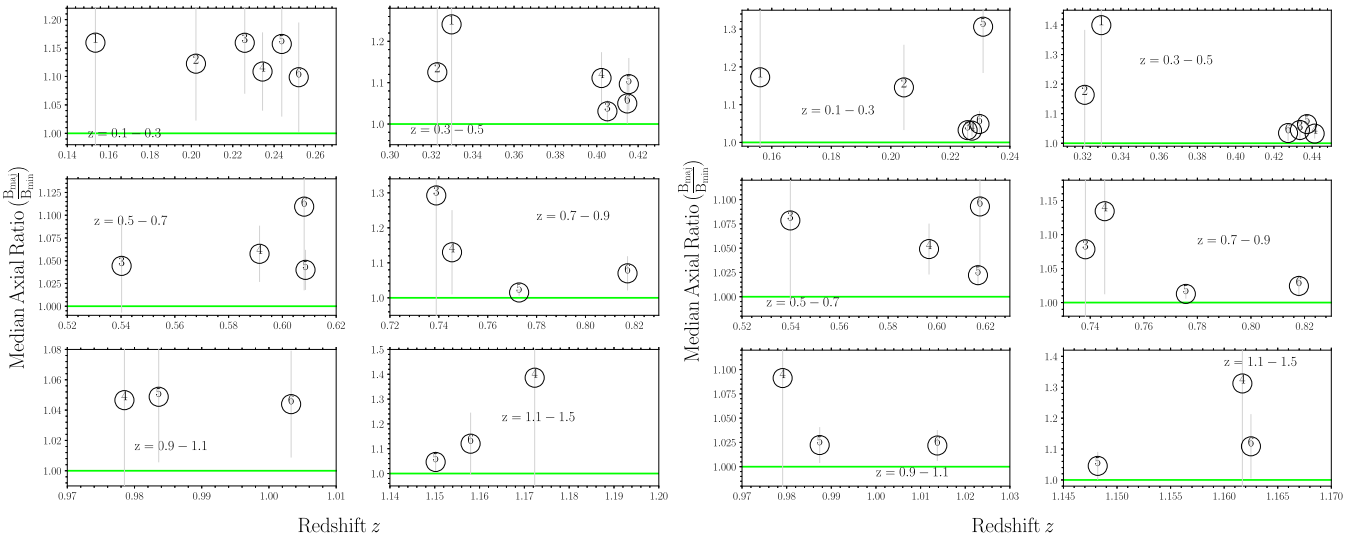

Figure 8. Stacked median axial ratio B_{maj}/B_{min} as a function of median redshift for all galaxies (left) and SFGs (right) represented as open black circles in each redshift bin. The horizontal solid green line represents the original axial ratio of the 610 MHz image, where $B_{maj}/B_{min} = 1$. The corresponding stellar mass bins (see Figs 4, 5, and 6) in each redshift range are shown as numbers (i.e. 1–6, from low to high stellar mass bins) in the middle of each open black circle. The sources shown here are from the median stacked images that show a clear detection at their centre from which we obtain Gaussian fits using PYBDSF source finder. Notice that these sources coincide with having a median stacked flux density with SNR ≥ 5.0 and in most cases above the mass completeness limit.

4.2 Estimating the radio star formation rates (SFR, Ψ)

Here, we calculate the radio luminosity (radio power) of the median stacked images and use it to estimate the radio-based SFRs.

The radio spectrum can be assumed to follow a simple power law ($S_\nu \propto \nu^\alpha$) resulting from the sum of the non-thermal synchrotron and thermal bremsstrahlung components; the power-law index is typically $\alpha \approx -0.8$ for SFGs (Condon 1992; Galvin et al. 2016). AGN-dominated sources may have steeper spectral indices (Ibar et al. 2009).

The observed stacked fluxes were converted to rest-frame (emitted) monochromatic luminosities using equation (4), which contains a bolometric *K-correction K(z)*:

$$L_{610} = 4\pi d_L^2 S_{610} K(z)[1+z]^{-1}. \quad (4)$$

Following the approach by Bourne et al. (2011), *K(z)*, that accounts for the shift of the spectrum in relation to the receiver, assuming a simple power-law spectrum to a monochromatic flux is given $K(z) = [1+z]^{-\alpha}$ where $\alpha = -0.8$.

Bell (2003) estimated the SFR, (Ψ), from 1.4 GHz luminosity of galaxies, calibrated from the total IR SFR for galaxies with $L \leq L^\star$ (defined as having an IR luminosity $L_{IR} \sim 2 \times 10^{10} L_\odot$). We followed Garn et al. (2009), and converted this relationship to a 610 MHz equivalent:

$$\left(\frac{\Psi}{M_\odot yr^{-1}}\right) = 2.84 \times 10^{-22} \left(\frac{L_{610}}{WHz^{-1}}\right). \quad (5)$$

For $L_{610} > L_c$ (where $L_c = 3.3 \times 10^{21}$ WHz^{-1} is the luminosity at 610 MHz of a $\sim L_\star$ galaxy, with $\Psi \simeq 1 M_\odot$ yr^{-1}), we can rewrite equation (5) as

$$\left(\frac{\Psi}{M_\odot yr^{-1}}\right) = \frac{2.84 \times 10^{-22}}{0.1 + 0.9(L_{610}/L_c)^{0.3}} \left(\frac{L_{610}}{WHz^{-1}}\right). \quad (6)$$

The left-hand and right-hand panels of Fig. 9 show the distribution of the stacked total and SFGs as a function of redshift, $M_\star$, and stacked radio power (L_{610} MHz). The x and y axes represent the $z - M_\star$ plane, while the z-axis sets the L_{610} MHz colour-coded by their derived SFR_{radio}. The relationship given by equations (5) and (6) is used to compute the stacked SFR_{radio}, Ψ.

Since the SFR is correlated with the stellar mass, a useful quantity to describe the SF regime of a galaxy is its sSFR, i.e. the SFR divided by the median stellar mass of the galaxies in the bin.

$$sSFR \equiv \frac{\Psi}{M_\star} \quad (7)$$

To explore the specific star formation we used the measured radio SFR from the median radio stack divided by the stellar mass. We follow the stellar mass and redshift bins described in Section 4.1.

4.3 Separation of sSFR dependence

The MS for SFGs correlation reveals interesting mechanisms of the star formation history (Brinchmann et al. 2004; Salim et al. 2007). The MS for SFGs has near-constant slope but shifts towards higher SFRs as the redshift increases (see e.g. Rodighiero et al. 2011; Johnston et al. 2015). We quantify the relationship between the sSFR and each of $M_\star$ and z, following Karim et al. (2011).

$$sSFR(M_\star, z) \propto sSFR(M_{\star|z}) sSFR(z|M_\star) = M_\star^\beta (1+z)^n \quad (8)$$

We fit the stacked sSFR $-$ $\log_{10} M_\star$ relation with these two separate functions of $M_\star$ and z.

$$sSFR(M_\star|z) = c_M(z) M_\star^\beta \quad (9)$$

We refer to the index β also as a slope since the relation is commonly shown in log space.

$$sSFR(z|M_\star) = c_z(M_\star)(1+z)^n \quad (10)$$

In subsequent sections, we examine the relationship between sSFR, $M_\star$, and z. We performed bootstrap linear regression fits to

Downloaded from https://academic.oup.com/mnras/article/524/4/5229/7227354 by Western Cape University user on 25 April 2024

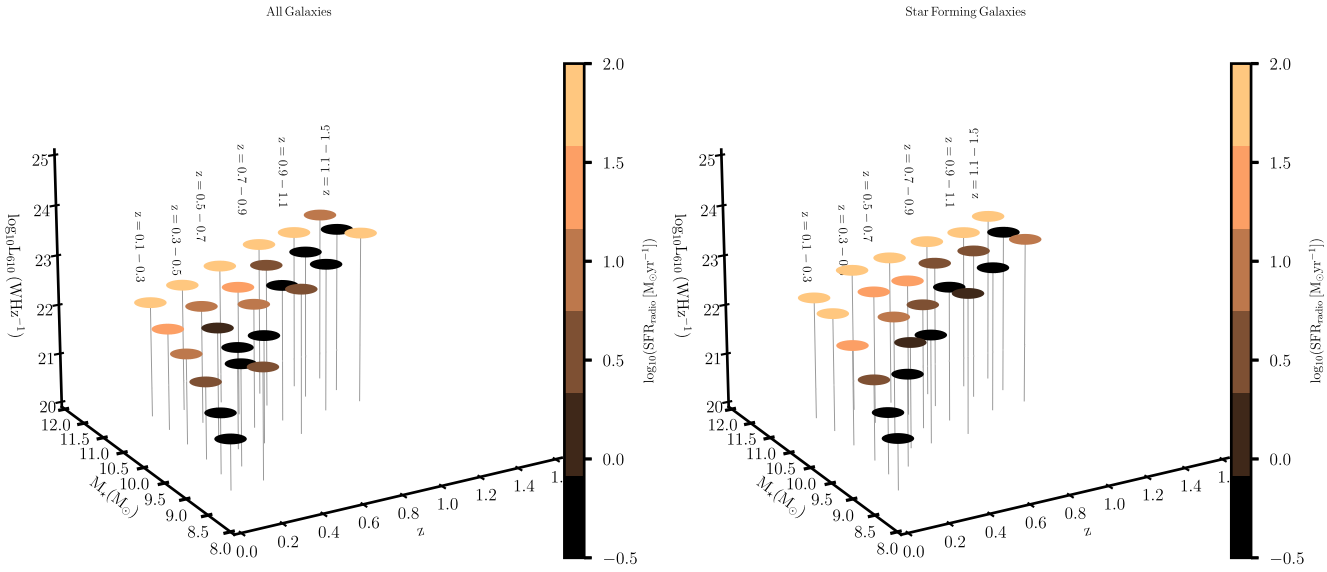

Figure 9. Left: Distribution of the total galaxies as a function of $M_\star$, redshift and stacked radio power at 610 MHz ($L_{610,\mathrm{MHz}}$), colour coded by the derived stacked $\mathrm{SFR_{radio}}$. Right: Distribution of the star-forming driven sources as a function of $M_\star$, redshift and stacked radio power at 610 MHz ($L_{610,\mathrm{MHz}}$), colour coded by the derived stacked $\mathrm{SFR_{radio}}$.

each sample.[2] The dashed lines in Figs 10 and 11 depict the best fit to the data in the mass representative β and redshift n regimes. In our bootstrap linear regression, we do not account for uncertainties associated with the SFR calibration, the photometric redshift, and stellar mass estimates as the large number of objects stacked for each data point ensures that even the joint error budget is statistically reduced to a low level that would not substantially enhance our uncertainty ranges (see Karim et al. 2011). We resampled the data set 1000 times to create new data sets with the same size as the original, and then fitting a linear regression model to each of the resampled data sets.

4.4 Dependence on stellar mass

In Fig. 10, we show the dependence of sSFR on stellar mass for all galaxies and SFG samples. The mass evolution of the sSFRs is well described by a power-law $(\mathrm{M_\star}|\mathrm{z}) \propto \mathrm{M_\star^\beta}$, as depicted by the solid dashed lines in Fig. 10. We first consider the whole sample that we refer to as all galaxies and show the redshift-dependent radio-based sSFRs that are distributed in the logarithmic sSFR − $\mathrm{M_\star}$ plane. We utilize sources that are above the mass completeness limit in our fitting. At a given redshift, the sSFR declines with increasing stellar mass for all galaxies. For $z \in [0.1 - 0.3]$, the value of the slope $\beta_{\mathrm{ALL}} = -0.47 \pm 0.01$. For the redshift bin $z \in [0.3 - 0.5]$, we measure the values of the slopes to be $\beta_{\mathrm{ALL}} = -0.58 \pm 0.01$. At $z \in [0.5 - 0.7]$, we measure the values of the slopes to be $\beta_{\mathrm{ALL}} = -0.51 \pm 0.02$. For $z \in [0.7 - 0.9]$, the value of the slope is $\beta_{\mathrm{ALL}} = -0.41 \pm 0.02$. For $z \in [0.9 - 1.1]$, we measure $\beta_{\mathrm{ALL}} = -0.41 \pm 0.02$.

For the SFG population, we measure $\beta_{\mathrm{SFG}} = -0.32 \pm 0.05$ and $\beta_{\mathrm{SFG}} = -0.50 \pm 0.01$ for the first and second redshift bins, respectively. For reshift bins $z \in [0.5 - 0.7]$ and $z \in [0.7 - 0.9]$, we measure $\beta_{\mathrm{SFG}} = -0.42 \pm 0.02$ and $\beta_{\mathrm{SFG}} = -0.41 \pm 0.01$, respectively. We measure $\beta_{\mathrm{SFG}} = -0.47 \pm 0.03$ for the fifth redshift bin. We can also infer from the second panel of the plot that the general trend of sSFR decreases with increasing stellar mass for the SFG population.

The 'mass gradient' for all galaxies and the SFG sample, i.e. β_{ALL} and β_{SFG}, is negative in all cases. The steepness of the sSFR with stellar mass is higher at high redshifts for both populations. If we ignore the highest redshift bin, for which the slope is poorly constrained, there is a consistent indication that the slope of the relation between sSFR and stellar mass becomes steeper with increasing redshift for both the total and SFG population. Our results of the individual fits to our data yielding the parameter β for all and SF galaxies are presented in Table 3. Fits have only been applied if more than two data points remained above the mass limit where the individual sample is regarded mass representative.

We observe that the sSFR is only weakly dependent on stellar mass, with sSFR decreasing as stellar mass increases that is consistent with previous work. Our radio-derived SFR provides a better match to the observed trends in sSFR versus stellar mass in the lowest mass bins, and also in reproducing the low redshift sSFR seen in other wavebands.

4.5 Dependence on redshift

Observational values for sSFR $\propto (1 + \mathrm{z})^{\mathrm{n}}$ may vary from $n = 2 - 5$ (see Salim et al. 2007; Karim et al. 2011; Popesso et al. 2019a). Results from non-stacked sample by Speagle et al. (2014) indicate that the sSFR evolves with redshift according to a factor of $(1 + z)^{2.5}$ (we provide a detailed comparison with sSFRs derived from other studies in Section 5.1). By plotting the same data as a function of redshift rather than in stellar mass classes an evolutionary trend is readily apparent. Fig. 11 indicates how sSFRs for our samples evolve with redshift. It is immediately evident that there is a dramatic increase sSFR by a factor of >100 over the interval $0.1 \leq \mathrm{z} \leq 1.5$. This is evident at all masses apart from the lowest

[2]A resampling method used to estimate the variability of statistical parameters from a data set that is repeatedly sampled with replacement (Lopes, Wang & Mahoney 2019).

Downloaded from https://academic.oup.com/mnras/article/524/4/5229/7227354 by Western Cape University user on 25 April 2024

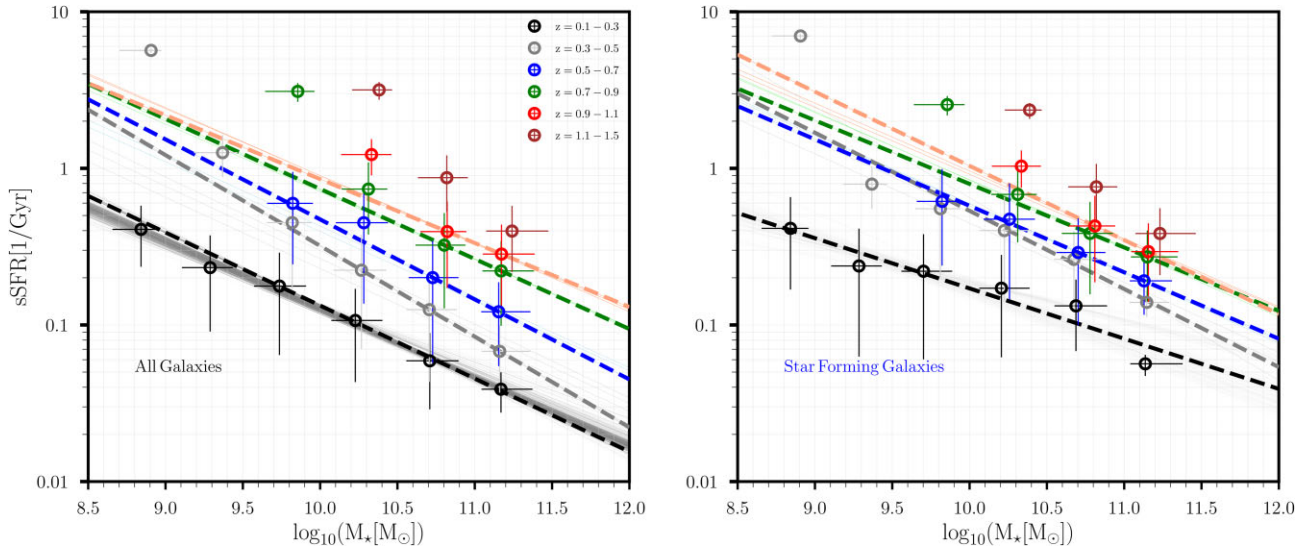

Figure 10. Radio-stacking based measurement of the sSFR as a function of redshift at a given stellar mass for all galaxies (left) and SFGs (right). Redshift ranges from $0.1 \leq z \leq 1.5$. Dashed lines are two-parameter fits of the form $c \times (M_\star/10^{11}M)^\beta$ to the mass-representative depicted by open circles. Horizontal bars indicate the width of those bins, while the vertical error bars simply reflect the Poisson uncertainties using the prescription of Gehrels (1986). The linear regression line that we get from each bootstrap replicate of the fit to each population as a function of mass are shown as black, grey, blue, red, and brown lines following each redshift bin.

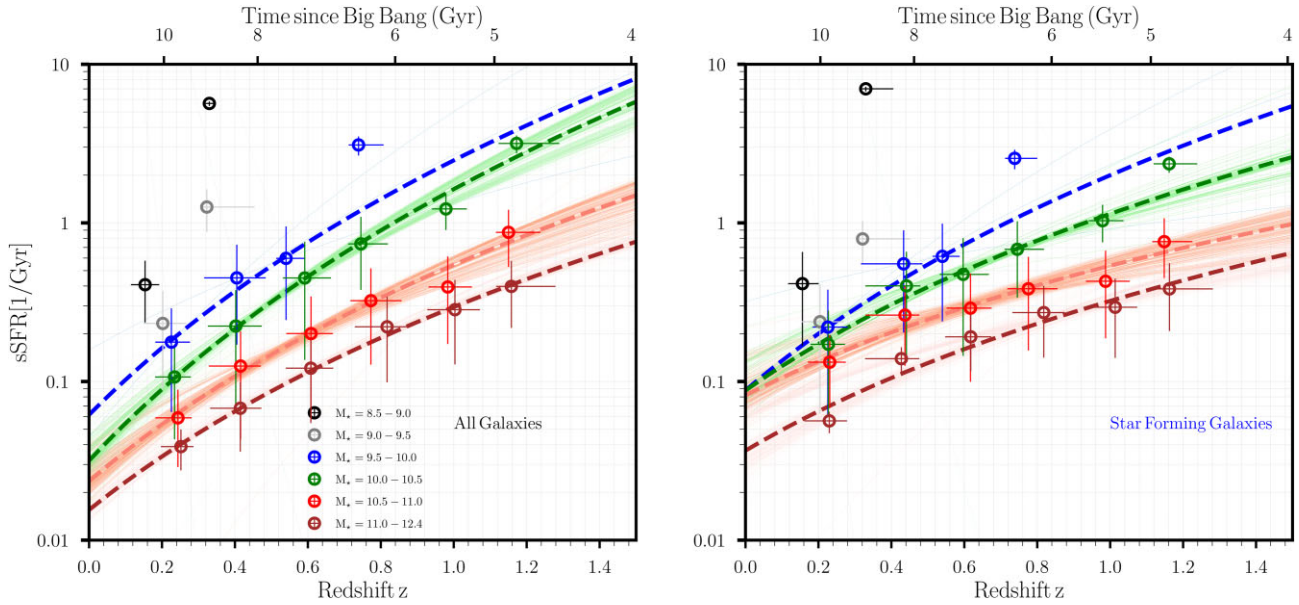

Figure 11. Radio-stacking based measurement of the sSFR as a function of stellar mass at a given redshift for all galaxies (left) and SFGs (right). Mass ranges from $10^{8.5} < M_\star/M_\odot < 10^{12.4}$. Two-parameter fits of the form $c \times (1+z)^n$ are applied the open circles that are representative samples for the underlying galaxy population. The error bars follows that of Fig. 10.

mass bin that has poor statistics and spans a limited redshift range. The redshift evolution of the sSFRs is well described by a power-law $(z|M_\star) \propto (1+z)^n$ as depicted by the solid dashed lines in Fig. 11 for a given mass bin. The simple power-law fit provides a good description of the data in most cases. The most massive galaxies have the lowest sSFR, at all epochs for both the total and SFG population. We do not show the fits for mass range $M_\star \in [8.5-9.0]$ & $[9.0-9.5]$ because of incompleteness in these bins. For $M_\star \in [9.5-10.0]$, the value of the slope $n_{\rm ALL} = 5.33 \pm 1.51$, whereas $n_{\rm SFG} = 4.50 \pm 1.36$. At $M_\star \in [10.0-10.5]$, the slope value increases to $n_{\rm ALL} = 5.69 \pm 0.26$ and $n_{\rm SFG} = 3.70 \pm 0.15$, respectively. For $M_\star \in [10.5-11.0]$, we measure $n_{\rm ALL} = 4.51 \pm 0.27$ and $n_{\rm SFG} = 2.71 \pm 0.25$, respectively. At the last mass bin, $M_\star \in [11.0-12.4]$, we measure slopes of $n_{\rm ALL} = 4.25 \pm 0.07$ and $n_{\rm SFG} = 3.13 \pm 0.34$, respectively. The redshift-evolution parameter n is slightly higher for all galaxies than for the SFG sample (i.e. $n_{\rm ALL} > n_{\rm SFG}$). This implies that at a given stellar mass, redshift evolution is stronger for the full sample than for the SFG sample. Our results of the individual fits to our data yielding the parameter n for all and SF galaxies are presented in Table 4. Fits have only been applied if more than two data points remained

Downloaded from https://academic.oup.com/mnras/article/524/4/5229/7227354 by Western Cape University user on 25 April 2024

Table 3. Table summarizing the two parameter fits to the mass dependence of the sSFR. We applied a power-law fit of the form $c \times (M_\star/10^{11}M)^\beta$ (equation 9, see also Karim et al. 2011) to the radio-stacking-based sSFRs as a function of mass within any redshift slice. All the slopes have been computed in a mass complete range.

	All galaxies		SFGs	
$\triangle z$	$\log(C_{M,\,All}[1/Gyr])$	β_{ALL}	$\log(C_{M,\,SFG}[1/Gyr])$	β_{SFG}
$0.1-0.3$	-1.34 ± 0.10	-0.47 ± 0.01	-1.08 ± 0.53	-0.32 ± 0.05
$0.3-0.5$	-1.07 ± 0.06	-0.58 ± 0.01	-0.77 ± 0.09	-0.50 ± 0.01
$0.5-0.7$	-0.83 ± 0.11	-0.51 ± 0.02	-0.66 ± 0.11	-0.42 ± 0.02
$0.7-0.9$	-0.57 ± 0.09	-0.45 ± 0.01	-0.50 ± 0.05	-0.41 ± 0.01
$0.9-1.1$	-0.47 ± 0.12	-0.41 ± 0.02	-0.45 ± 0.07	-0.47 ± 0.03
$1.1-1.5$	–	–	–	–
	$\langle\beta\rangle$ =	-0.49 ± 0.01	$\langle\beta\rangle$ =	-0.42 ± 0.02

Table 4. Table summarizing the two parameter fits to the redshift evolution of the sSFR. We applied a power-law fit of the form $c \times (1+z)^n$ (equation 10) to the radio-stacking-based sSFRs as a function of redshift within any mass bin.

	All galaxies		SFGs	
$\triangle\log(M_\star[M_\odot])$	$\log(C_{z,\,All}[1/Gyr])$	n_{ALL}	$\log(C_{z,\,SFG}[1/Gyr])$	n_{SFG}
$8.5-9.0$	–	–	–	–
$9.0-9.5$	–	–	–	–
$9.5-10.0$	-1.21 ± 0.15	5.33 ± 1.51	-1.06 ± 0.12	4.50 ± 1.36
$10.0-10.5$	-1.50 ± 0.03	5.69 ± 0.26	-1.06 ± 0.04	3.70 ± 0.15
$10.5-11.0$	-1.63 ± 0.04	4.51 ± 0.27	-1.09 ± 0.05	2.71 ± 0.25
$11.0-12.4$	-1.81 ± 0.01	4.25 ± 0.07	-1.44 ± 0.09	3.13 ± 0.34
	$\langle n\rangle$ =	4.94 ± 0.53	$\langle n\rangle$ =	3.51 ± 0.52

above the mass limit where the individual sample is regarded mass representative.

5 DISCUSSION

Our results of the sSFR–mass relation steepening with redshift are in broad agreement with those based on far-IR stacking experiments that found almost flat relations up to $z\sim1.5$.

On the whole, there is a good agreement between our fits and recent work, mostly probing high-z observations. This is justification that our fits as functions of redshift with a power law do provide nearly as good fits compared to the literature. We are not able to definitively rule out a possible 'plateauing' of the sSFR in the redshift range explored here. In inference, our results seem to favour a scenario where the sSFRs will continue to increase until at least $z\sim3$, as found by studies from the literature, if we were to probe a broader redshift range. Redshift dependence of the sSFR $-$ $M_\star$ relation is more uncertain (Ilbert et al. 2013; Schreiber et al. 2015; Pearson et al. 2018) and studying the redshift evolution of these different populations through stacking thus provide complementary insights into the host properties of these sources. In this section, we discuss our results and compare with sSFRs derived from other studies including those from radio-stacking experiments.

5.1 Comparison with β and n of sSFRs derived from previous studies

We compare our results to those previous studies conducted at 1.4 GHz and the authors have considered more than one SFR indicator. In Sections 4.4 and 4.5, we found that sSFR decreases with stellar mass (downsizing; see Fig. 10) and increases with redshift (see Fig. 11) for all galaxies and SFG populations. Additionally, β_{ALL} and β_{SFG} for the dependence on stellar mass are all negative whereas their values become steeper with increasing redshift. Radio-based measurements of the sSFR–$M_\star$ relation have been studied by previously in the literature.

We compare with our measurements with the mass dependent slope estimates from Karim et al. (2011) and Zwart et al. (2014). The top panel of Fig. 12 presents the comparison of gradient β against stellar mass as a function of redshift for the total (left) and the SFG population (right). These studies form the literature and our work share some methodological similarities (e.g. the use of a mass and K-selected samples and a radio-stacking approach) and should therefore be directly comparable. However, there are some technical differences in the exact implementation of the image stacking as already discussed (see Section 4.1). It is important to also point out that the calibration of the individual radio SFRs and binning of this work are different from these previous studies. However, in terms of the evolution of the sSFR sequence both studies show a reasonable agreement with our work. The differences that arise may be attributed to our study tracing 610 MHz rather than 1.4GHz, which these past studies were conducted.

Karim et al. (2011) concluded that the sSFR sequence itself tends to flatten towards lower masses and $z>1.5$. They inferred this might be explained by an upper limiting threshold where average SF systems already reach levels of star formation that qualify them to double their mass within a dynamical time. Their data show that there is a tight correlation with power-law dependence, $\mathrm{sSFR}\propto M_\star^\beta$, between sSFR and stellar mass at all epochs. Excluding QGs from their analysis, a shallow index $\beta_{SFG}\approx-0.4$ fits the correlation for star-forming sources. For their total population the sSFR–mass gradient β becomes steeper with $\beta_{ALL}\approx-0.67$. The sSFR–mass gradients β found by Zwart et al. (2014) become less steep with redshift (from $\beta\approx-0.75$ to $\beta\approx-0.25$ out to $z\simeq2$) for the full and

Downloaded from https://academic.oup.com/mnras/article/524/4/5229/7227354 by Western Cape University user on 25 April 2024

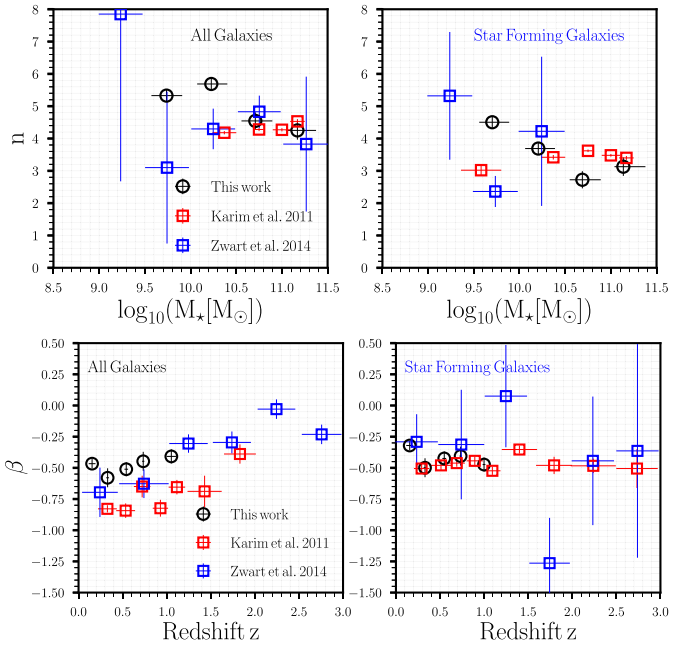

Figure 12. Top: Comparison of gradient β against stellar mass as a function of redshift for the total (left) and the SFG population (right). The open red squares represent measurements from Karim et al. (2011), whereas the open blue squares represent measurements from Zwart et al. (2014). Bottom: Comparison of redshift evolution parameter of n sSFR as a function of stellar mass for all galaxies (left-hand panel) and the SFG population (right-hand panel).

elliptical samples, but show no dependence with redshift ($\beta \approx -0.5$) for the starburst and irregular galaxies for their stacked deep (17.5 μJy) VLA radio observations.

Studies based on IR SFRs such as Rodighiero et al. (2010) found that the sSFR–mass relation steepens with redshift for all galaxies, becoming almost flat at $z < 1.0$ and reaching a slope of $n = -0.50^{+0.13}_{-0.16}$ at $z \sim 2$. Moreover, they also show that the most massive galaxies have the lowest sSFRs at any redshift. Further implying that they have formed their stars earlier and more rapidly than their low-mass counterparts that correspond with our findings. Oliver et al. (2010) in their analysis of sSFR activity of galaxies and their evolution near the peak of the cosmic far-IR background at 70 and 160 μm found a trend sSFR $\propto M^{\beta}_{star}$ with $\beta \sim -0.38$. They found a stronger trend for early-type galaxies ($\beta \sim -0.46$) than late-type galaxies ($\beta \sim -0.15$).

The bottom panel of Fig. 12 shows a comparison of the redshift evolution parameter recorded of n sSFR as a function of stellar mass for all galaxies (left) and the SFG (right) population derived from Fig. 11. Although we observe that all measured sSFRs (i.e. total galaxies and SFG) increase with redshift, massive galaxies have the lowest sSFRs. The sSFRs span a smaller range at high redshift, with massive galaxies evolving faster compared to low-mass galaxies, decreasing their sSFR at earlier epochs. Our results are in broad agreement with those based on radio-stacking that find almost flat relations up to $z \sim 2$ (see Dunne et al. 2009; Pannella et al. 2009). Karim et al. (2011) noted that at redshift $0.2 < z < 3$ both populations show a strong and mass-independent decrease in their sSFR towards the present epoch where $n \sim 4.3$ for all galaxies and $n \sim 3.5$ for star-forming sources. Zwart et al. (2014) reported that the redshift evolution of sSFR is much faster for their full sample than their starburst sample. Oliver et al. (2010) found that the sSFR evolves as $(1 + z)^n$ with $n = 4.4 \pm 0.3$ for galaxies with $10.5 < \log_{10} M_{\star}/M_{\odot} < 12.0$. For early-type galaxies, they found that the average evolution in this mass range is stronger ($n \sim 5.7$) but decreases to higher mass.

Our SFG sample comprises sources that do not satisfy QG criterion, spectroscopically identified as AGN, satisfies the Donley et al. (2012) IR AGN criterion, and have an X-ray counterpart. This does not explicitly make our sample immune from AGN contamination. It is expected that AGNs reside in massive SFGs (see Kauffmann et al. 2003; Mullaney et al. 2012; Juneau et al. 2013; Rosario et al. 2013). As such, AGN contamination could be a major reason to doubt that 610 MHz radio emission might be a reliable star formation tracer. Padovani (2017) emphasizes that for flux density $\lesssim$1 mJy, the faint radio sky is populated by both non-jetted AGNs and a quickly decreasing fraction of jetted AGNs (see also Padovani 2016). Studies by Daddi et al. (2007) conducted at mid- and far-IR to submillimetre, radio, and rest-frame UV wavelengths, measured contamination to SFRs from X-ray-emitting AGNs. They used radio stacking to investigate trends for radio undetected sources and found that the L_{IR} estimated from 24 μm exceeds on average by an order of magnitude the same quantity derived from radio. This was attributed to the additional radio emission from an AGN, as suggested also by Donley et al. (2007), mostly in low-redshift galaxies. Ji et al. (2022) highlighted the importance AGN selection effects on the distributions of host galaxy properties. They combined a study of X-ray and IR AGN at $z \approx 2$ and compared the star formation and morphological properties of AGN and non-AGN host galaxies. Their studies revealed that non-AGN SFGs on the main sequence and X-ray AGN have similar median star formation properties. Classification of sources as either SFG or AGN, appears to be a more complex problem and in reality, not all sources will give unambiguous results over all criteria. Hence, we do not reject AGN contamination contribution argument to the radio emission in the selected SFGs. Studies by Ito et al. (2022) reveal that the frequency of AGN hosted by transitional, from SFGs to QGs, depends significantly on how the AGNs are selected.

Downloaded from https://academic.oup.com/mnras/article/524/4/5229/7227354 by Western Cape University user on 25 April 2024

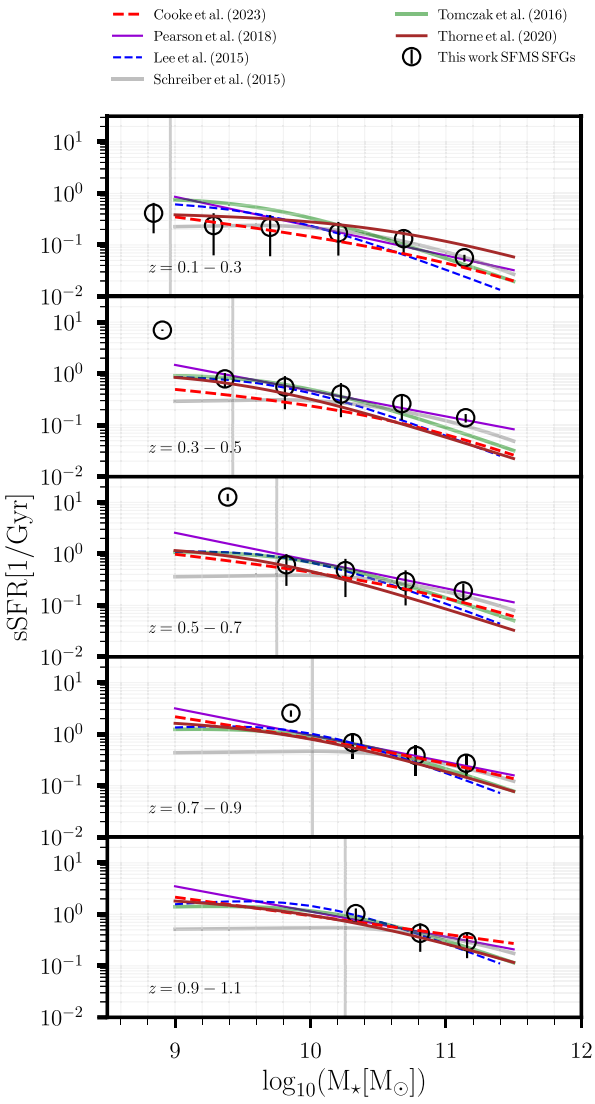

Figure 13. Comparison of the radio-stacked based measurement of sSFR for SFGs to the MS trends observed by Lee et al. (2015), Schreiber et al. (2015), Tomczak et al. (2016), Pearson et al. (2018), Thorne et al. (2021), and Cooke et al. (2023), shown in each panel as dash blue curves, solid grey curves, solid violet lines, solid green curves, solid brown curves, and dash red curves, respectively. The solid grey vertical lines in each panel represents the mass completeness limit, $M_{\rm lim}$.

In summary, our measurements for both the sSFR–mass and sSFR–redshift evolution are largely consistent between the VIDEO (i.e. Zwart et al. 2014), COSMOS (i.e. Karim et al. 2011), and our 610 MHz GMRT data set of the ELAIS-N1. Although for the sSFR–redshift evolution parameter, n, we measure slightly higher in our data. We also measure slightly steeper mass gradient, β.

5.2 Comparison of our MS for SFGs to previous studies

The UV, IR, and radio wavelengths have been used to characterize the star formation properties for different classes of sources in literature, by investigating their SFRs. We provide in Fig. 13 a comparison of the our radio-stacked based measurement of sSFR evolution with other works in literature. We compare the evolution of the sSFR derived for five different redshift bins to the MS trends observed by other studies in the literature. These measurements from previous studies were conducted in the SFR–$M_\star$ plane. To illustrate the scientific value of our stacked data, we convert to the sSFR–$M_\star$ plane in order to easy comparison. The solid grey vertical lines in each panel represents the mass completeness limit, $M_{\rm lim}$, above which we perform the fitting in Sections 4.4 and 4.5. Lee et al. (2015) used rest-frame colour–colour diagram ($NUV - r$) versus ($r - K$), to study the MS in the COSMOS field at $0.3 < z < 1.3$. Schreiber et al. (2015) conducted stacking analysis of *UVJ* selected galaxies in the deep Herschel PACS maps of the CANDELS fields. They demonstrated that galaxies at $z = 4$ to 0 of all stellar masses follow the MS for SFGs. Tomczak et al. (2016) performed stacking analysis of *UVJ* selected galaxies combining mean IR luminosity with mean *NUV* luminosity to derive SFR. We compare their fits, solid green curves, in similar redshift range to our stacked points. Pearson et al. (2018) selected SFGs following the *UVJ* selection as in Whitaker et al. (2014) and traced the MS over $0.2 \leq z < 6.0$ and $10^{9.0} < M_\star/{\rm M}_\odot < 10^{11.0}$. Their simple two-parameter power-law fits are shown as solid violet lines in each panel in Fig. 13. Thorne et al. (2021) used multiwavelength photometry from the *Deep Extragalactic VIsible Legacy Survey* (DEVILS; Davies et al. 2018) and measured stellar masses and SFR for galaxies in the COSMOS field mapping the evolution of the SFR–$M_\star$ relation for $0 < z < 4.25$ redshift range. Their fits, which is obtained by adapting the parametrization from Lee et al. (2015) and adding an slope to freely model SFR at high stellar masses are shown as solid brown curves. Cooke et al. (2023) investigated the relationship between SFR–$M_\star$ of SFGs in the COSMOS field from $0 < z < 3.5$. The fitted MS curves measured from their construction of FUV–FIR SEDs of stellar mass-selected sample are shown in the individual panels of Fig. 13 as dash red curves. We adopt the Chabrier (2003) IMF since all but the Schreiber et al. (2015) data points used this IMF. In the case of Schreiber et al. (2015) who applied a Salpeter (1955) IMF, we multiplied by constant factors of $0.62M_{\star,S}$ to convert to Chabrier. Deep and wide-area radio surveys, such as our 610 MHz data, are powerful tools to study a range of source populations. These comparisons demonstrate that the measurements from the literature are consistent with our derived radio-stacked measurements for SFGs. Similar to the IR, the radio emission at 610 MHz is equivalently a good tracer of the SFR in SFGs.

6 CONCLUSIONS AND FUTURE WORK

We combined deep multiwavelength optical and IR observations from the LoTSS survey with deep 610 MHz GMRT observations to conduct a stacking analysis of SFGs between $0.1 \leq z \leq 1.5$. The depth of our 610 MHz data represents a potentially very useful tool to address the role of SFGs in galaxy evolution. We have stacked deep, below the ∼40 μJy sensitivity of the 610 MHz GMRT radio observations at the positions of K-selected sources in the ELAIS-N1 field (for K band < 22.7, sensitive to $0.1 \leq z \leq 1.5$). We remove source QGs, and suspected of hosting active AGNs from all samples based on optical, X-ray, and IR indicators. Using median image stacking technique that is best applied in the radio regime where the angular resolution is high, we have measured stellar mass-dependent average SFRs in the redshift range $0.1 \leq z \leq 1.5$. Our principal findings can be summarized as follows:

(i) We use a combination of rest-frame $u - r$ colour, optical spectroscopy, X-ray information, and IR colours to separate QGs and AGN-driven sources from SFGs of redshift and mass-selected galaxies.

Downloaded from https://academic.oup.com/mnras/article/524/4/5229/7227354 by Western Cape University user on 25 April 2024

(ii) We used median single-pixel stacking, converting the stacked radio fluxes to SFRs. We apply the Bell (2003) relationship between radio luminosity and SFR, calibrated from local galaxies, and successfully apply it to high-redshift, high-SFR galaxies, and for the first time study the relationship between radio stacked sSFR, stellar mass and redshift using deep 610 MHz data.

(iii) We subdivided our sample into stellar mass and redshift bins and fit the sSFRs as a separable function of stellar mass and redshift in each bin. We found that sSFR falls with stellar mass for both our full and SFG samples. Hence the 'downsizing' scenario is supported by our 610 MHz data because we measure $\beta < 0$, implying that galaxies tend to form their stars more actively at higher redshifts.

(iv) We report an average of mass slope $\langle\beta_{\rm All}\rangle = -0.49 \pm 0.01$ for all galaxies and $\langle\beta_{\rm SFG}\rangle = -0.42 \pm 0.02$ for the SFG population.

(v) We report a strong increase of the sSFR with redshift, for a given stellar mass, that is best parametrized by a power-law $\propto (1 + z)^{4.94}$ for all galaxies. The SFG population is best parametrized by a power-law $\propto (1 + z)^{3.51}$.

(vi) The sSFR appears to flatten at $z > 1.0$ for $M_\star > 10^{10.5}\,{\rm M}_\odot$. The sSFR$-M_\star$ relation that is steeper at low masses than at high masses (i.e. a flattening is present). Furthermore, that most massive galaxies in both the full sample and the SFG sample consistently exhibit the lowest sSFRs at all redshifts.

(vii) We compare our stacked sSFR estimates to previous measurements in the sSFR–$M_\star$ plane, and the evolution of the MS. We find good agreement with these previous measurements. This result opens the possibility of using the radio bands at low frequency to estimate the SFR even in the hosts of QGs and bright AGNs.

In view of the wealth of multiwavelength information provided by the LoTSS catalogue, there still exist significant opportunities to expand this work. A more comprehensive science analysis through stacking will include:

(i) Surveys at low frequencies, where extensive surveys exist, present different and complementary views on radio sources to that of high frequency surveys. We aim to further compare our findings at 610 MHz, with results from LOFAR 150 MHz.

(ii) To undertake the exploitation of the radio luminosity functions of these distinct galaxy populations measured above and below the detection threshold of these surveys, using a Bayesian model-fitting technique. Extending this technique to study the cosmic SFR density at high redshifts.

Future radio surveys will be dominated by galaxies substantially fainter than those in this current sample. The prospects for studying the faint radio sky are very bright, as we are being rapidly flooded with survey data by SKA pathfinders. In conjunction with other multiwavelength facilities, such as *Euclid* (Amendola et al. 2018) and the Vera C. Rubin Legacy Survey of Space and Time (*LSST*; Ivezić et al. 2019), these projects that will survey the sky vastly faster than it is possible with existing radio telescopes.

ACKNOWLEDGEMENTS

We would like to thank the anonymous referee for their careful comments that led to a highly improved paper. This research was supported by the Korea Astronomy and Space Science Institute under the R&D program (Project No. 2022186804) supervised by the Ministry of Science and ICT. JMS acknowledges the support of the Natural Sciences and Engineering Research Council of Canada (NSERC), 2019–04848. CHIC acknowledges the support of the Department of Atomic Energy, Government of India, under the project 12-R&D-TFR-5.02-0700. EFO would like to acknowledge the hospitality of the Inter-University Institute for Data Intensive Astronomy (IDIA) that is a partnership of the University of Cape Town, the University of Pretoria, the University of the Western Cape, and the South African Radio Astronomy Observatory. MV acknowledges financial support from the Inter-University Institute for Data Intensive Astronomy (IDIA), a partnership of the University of Cape Town (UCT), the University of Pretoria, the University of the Western Cape, and the South African Radio Astronomy Observatory, and from the South African Department of Science and Innovation's National Research Foundation under the ISARP RADIOSKY2020 Joint Research Scheme (DSI-NRF grant number 113121) and the CSUR HELP-IDIA Panchromatic PrOject (HIPPO) Project (DSI-NRF grant number 121291). We acknowledge the use of the ilifu cloud computing facility – https://www.ilifu.ac.za, a partnership between the University of Cape Town, the University of the Western Cape, the University of Stellenbosch, Sol Plaatje University, the Cape Peninsula University of Technology, and the South African Radio Astronomy Observatory. The ilifu facility is supported by contributions from the Inter-University Institute for Data Intensive Astronomy (IDIA – a partnership between the UCT , the University of Pretoria, the University of the Western Cape and the South African Radio Astronomy Observatory), the Computational Biology division at UCT and the Data Intensive Research Initiative of South Africa (DIRISA). We thank Ben Keller for sharing his PASTA stacking code with us before its public release and for his helpful advice on the installation of the code on the ilifu cloud computing facility at the Inter-University Institute for Data Intensive Astronomy (IDIA).

This work relies on PYTHON programming language (https://www.python.org/) the Python Astronomical Stacking Tool Array (PASTA) program developed at the University of Calgary by Ben Keller and Jeroen Stil and is available at https://github.com/bwkeller/PASTA. We used ASTROPY (https://www.astropy.org/; Astropy Collaboration 2013, 2018), NUMPY (https://numpy.org/), and MATPLOTLIB (https://matplotlib.org/).

DATA AVAILABILITY

The derived stacked-radio data generated in this research will be shared upon reasonable request to the corresponding author. The LOFAR science-ready multiwavelength data, containing the details of the photometric redshift and stellar mass as provided in Duncan et al. (2021), is public and available at https://lofar-surveys.org/deepfields_public_en1.html.

REFERENCES

Algera H. S. B. et al., 2020, ApJ, 903, 139
Amendola L. et al., 2018, Living Rev. Relativ., 21, 2
Astropy Collaboration, 2013, A&A, 558, A33
Astropy Collaboration, 2018, AJ, 156, 123
Behroozi P. S., Wechsler R. H., Conroy C., 2013, ApJ, 762, L31
Bell E. F., 2003, ApJ, 586, 794
Bell E. F. et al., 2004, ApJ, 608, 752
Best P. N. et al., 2023, MNRAS, 523, 1729
Borch A. et al., 2006, A&A, 453, 869
Bourne N., Dunne L., Ivison R. J., Maddox S. J., Dickinson M., Frayer D. T., 2011, MNRAS, 410, 1155
Bourne N. et al., 2012, MNRAS, 421, 3027
Brammer G. B. et al., 2009, ApJ, 706, L173
Brinchmann J., Charlot S., White S. D. M., Tremonti C., Kauffmann G., Heckman T., Brinkmann J., 2004, MNRAS, 351, 1151
Bruzual G., Charlot S., 2003, MNRAS, 344, 1000

Downloaded from https://academic.oup.com/mnras/article/524/4/5229/7227354 by Western Cape University user on 25 April 2024

Carnall A. C. et al., 2019, MNRAS, 490, 417
Cassata P. et al., 2007, ApJS, 172, 270
Chabrier G., 2003, PASP, 115, 763
Charlot S., Fall S. M., 2000, ApJ, 539, 718
Cochrane R. K. et al., 2023, MNRAS, 523, 6082
Condon J. J., 1992, ARA&A, 30, 575
Condon J. J., Cotton W. D., Broderick J. J., 2002, AJ, 124, 675
Cooke K. C. et al., 2023, ApJ, 942, 49
Daddi E. et al., 2007, ApJ, 670, 156
Davidzon I. et al., 2013, A&A, 558, A23
Davidzon I. et al., 2017, A&A, 605, A70
Davidzon I., Ilbert O., Faisst A. L., Sparre M., Capak P. L., 2018, ApJ, 852, 107
Davies L. J. M. et al., 2018, MNRAS, 480, 768
Donley J. L., Rieke G. H., Pérez-González P. G., Rigby J. R., Alonso-Herrero A., 2007, ApJ, 660, 167
Donley J. L. et al., 2012, ApJ, 748, 142
Driver S. P., Robotham A. S. G., 2010, MNRAS, 407, 2131
Duncan K. et al., 2014, MNRAS, 444, 2960
Duncan K. et al., 2019, ApJ, 876, 110
Duncan K. J. et al., 2021, A&A, 648, A4
Dunne L. et al., 2009, MNRAS, 394, 3
Eddington A. S., 1913, MNRAS, 73, 359
Elbaz D. et al., 2007, A&A, 468, 33
Feulner G., Goranova Y., Hopp U., Gabasch A., Bender R., Botzler C. S., Drory N., 2007, MNRAS, 378, 429
Galvin T. J., Seymour N., Filipović M. D., Tothill N. F. H., Marvil J., Drouart G., Symeonidis M., Huynh M. T., 2016, MNRAS, 461, 825
Garn T., Alexander P., 2009, MNRAS, 394, 105
Garn T., Green D. A., Riley J. M., Alexander P., 2009, MNRAS, 397, 1101
Gehrels N., 1986, ApJ, 303, 336
Haarsma D. B., Partridge R. B., Windhorst R. A., Richards E. A., 2000, ApJ, 544, 641
Helou G., Soifer B. T., Rowan-Robinson M., 1985, ApJ, 298, L7
Ibar E., Ivison R. J., Biggs A. D., Lal D. V., Best P. N., Green D. A., 2009, MNRAS, 397, 281
Ilbert O. et al., 2013, A&A, 556, A55
Ishwara-Chandra C. H., Taylor A. R., Green D. A., Stil J. M., Vaccari M., Ocran E. F., 2020, MNRAS, 497, 5383
Ito K. et al., 2022, ApJ, 929, 53
Ivezić Ž. et al., 2019, ApJ, 873, 111
Ivison R. J. et al., 2007, MNRAS, 380, 199
Jarvis M. J. et al., 2013, MNRAS, 428, 1281
Jarvis M. et al., 2016, Proc. Sci., The MeerKAT International GHz Tiered Extragalactic Exploration (MIGHTEE) Survey. SISSA, Trieste, PoS#6
Ji Z., Giavalisco M., Kirkpatrick A., Kocevski D., Daddi E., Delvecchio I., Hatcher C., 2022, ApJ, 925, 74
Johnston R., Vaccari M., Jarvis M., Smith M., Giovannoli E., Häußler B., Prescott M., 2015, MNRAS, 453, 2540
Juneau S. et al., 2013, ApJ, 764, 176
Karim A. et al., 2011, ApJ, 730, 61
Kauffmann G. et al., 2003, MNRAS, 346, 1055
Keller B. W., Stil J. M., 2018, Astrophysics Source Code Library, record ascl:1809.003
Kondapally R. et al., 2021, A&A, 648, A3
Lacy M. et al., 2004, ApJS, 154, 166
Lacy M., Sajina A., Petric A. O., Seymour N., Canalizo G., Ridgway S. E., Armus L., Storrie-Lombardi L. J., 2007, ApJ, 669, L61
Laigle C. et al., 2016, ApJS, 224, 24
Lawrence A. et al., 2007, MNRAS, 379, 1599
Lee N. et al., 2010, ApJ, 717, 175
Lee N. et al., 2015, ApJ, 801, 80
Leja J. et al., 2019a, ApJ, 877, 140
Leja J., Tacchella S., Conroy C., 2019b, ApJ, 880, L9
Leslie S. K. et al., 2020, ApJ, 899, 58
Lopes M. E., Wang S., Mahoney M. W., 2019, J. Mach. Learn. Res., 20, 1
McCracken H. J. et al., 2012, A&A, 544, A156
Mohan N., Rafferty D., 2015, Astrophysics Source Code Library, record ascl:1502.007
Moster B. P., Somerville R. S., Newman J. A., Rix H.-W., 2011, ApJ, 731, 113
Mullaney J. R. et al., 2012, ApJ, 753, L30
Muzzin A. et al., 2013, ApJS, 206, 8
Noeske K. G. et al., 2007, ApJ, 660, L43
Norris R. P., 2011, J. Astrophys. Astron., 32, 599
Ocran E. F., Taylor A. R., Vaccari M., Ishwara-Chandra C. H., Prandoni I., Prescott M., Mancuso C., 2021, MNRAS, 500, 4685
Oliver S. et al., 2000, MNRAS, 316, 749
Oliver S. et al., 2010, MNRAS, 405, 2279
Oogi T. et al., 2022, preprint (arXiv:2207.14689)
Padovani P., 2011, MNRAS, 411, 1547
Padovani P., 2016, A&AR, 24, 13
Padovani P., 2017, Front. Astron. Space Sci., 4, 35
Pannella M. et al., 2009, ApJ, 698, L116
Patel S. G., Kelson D. D., Holden B. P., Franx M., Illingworth G. D., 2011, ApJ, 735, 53
Patel S. G., Holden B. P., Kelson D. D., Franx M., van der Wel A., Illingworth G. D., 2012, ApJ, 748, L27
Pearson W. J. et al., 2018, A&A, 615, A146
Peng Y.-j. et al., 2010, ApJ, 721, 193
Popesso P. et al., 2019a, MNRAS, 483, 3213
Popesso P. et al., 2019b, MNRAS, 490, 5285
Powell M. C., Urry C. M., Cardamone C. N., Simmons B. D., Schawinski K., Young S., Kawakatsu M., 2017, ApJ, 835, 22
Pozzetti L. et al., 2007, A&A, 474, 443
Pozzetti L. et al., 2010, A&A, 523, A13
Prandoni I., Gregorini L., Parma P., de Ruiter H. R., Vettolani G., Wieringa M. H., Ekers R. D., 2001, A&A, 365, 392
Randall K. E., Hopkins A. M., Norris R. P., Zinn P. C., Middelberg E., Mao M. Y., Sharp R. G., 2012, MNRAS, 421, 1644
Reddy N. A., Pettini M., Steidel C. C., Shapley A. E., Erb D. K., Law D. R., 2012, ApJ, 754, 25
Renzini A., Peng Y.-j., 2015, ApJ, 801, L29
Retana-Montenegro E., 2022, A&A, 663, A153
Rodighiero G. et al., 2010, A&A, 518, L25
Rodighiero G. et al., 2011, ApJ, 739, L40
Rosario D. J. et al., 2013, A&A, 560, A72
Sabater J. et al., 2019, A&A, 622, A17
Sabater J. et al., 2021, A&A, 648, A2
Salim S. et al., 2007, ApJS, 173, 267
Salpeter E. E., 1955, ApJ, 121, 161
Sandles L., Curtis-Lake E., Charlot S., Chevallard J., Maiolino R., 2022, MNRAS, 515, 2951
Schawinski K. et al., 2014, MNRAS, 440, 889
Schreiber C. et al., 2015, A&A, 575, A74
Serjeant S. et al., 2004, ApJS, 154, 118
Shimwell T. W. et al., 2017, A&A, 598, A104
Shimwell T. W. et al., 2019, A&A, 622, A1
Shimwell T. W. et al., 2022, A&A, 659, A1
Smolčić V. et al., 2017, A&A, 602, A6
Speagle J. S., Steinhardt C. L., Capak P. L., Silverman J. D., 2014, ApJS, 214, 15
Stanley F. et al., 2017, MNRAS, 472, 2221
Stern D. et al., 2005, ApJ, 631, 163
Stil J. M., Keller B. W., George S. J., Taylor A. R., 2014, ApJ, 787, 99
Straatman C. M. S. et al., 2014, ApJ, 783, L14
Straatman C. M. S. et al., 2016, ApJ, 830, 51
Thorne J. E. et al., 2021, MNRAS, 505, 540
Tomczak A. R. et al., 2016, ApJ, 817, 118
van Haarlem M. P. et al., 2013, A&A, 556, A2
Villarroel B., Korn A. J., 2014, Nat. Phys., 10, 417
Whitaker K. E. et al., 2011, ApJ, 735, 86
Whitaker K. E., van Dokkum P. G., Brammer G., Franx M., 2012, ApJ, 754, L29

Downloaded from https://academic.oup.com/mnras/article/524/4/5229/7227354 by Western Cape University user on 25 April 2024

Whitaker K. E. et al., 2014, ApJ, 795, 104
White R. L., Helfand D. J., Becker R. H., Glikman E., de Vries W., 2007, ApJ, 654, 99
Williams R. J., Quadri R. F., Franx M., van Dokkum P., Labbé I., 2009, ApJ, 691, 1879
Williams W. L. et al., 2019, A&A, 622, A2
Wuyts S., Labbé I., Förster Schreiber N. M., Franx M., Rudnick G., Brammer G. B., van Dokkum P. G., 2008, ApJ, 689, 653
Wuyts S. et al., 2011a, ApJ, 738, 106
Wuyts S. et al., 2011b, ApJ, 742, 96
Yun M. S., Reddy N. A., Condon J. J., 2001, ApJ, 554, 803
Zwart J. T. L., Jarvis M. J., Deane R. P., Bonfield D. G., Knowles K., Madhanpall N., Rahmani H., Smith D. J. B., 2014, MNRAS, 439, 1459

APPENDIX A: THE COLOUR–MASS DIAGRAM

In Fig. A1, we show the colour–mass distribution diagram same as Fig. 3. We show the red and blue sequence splitting lines analogous to Borch et al. (2006) redshift evolution up to $z = 1.5$ as grey solid lines in each panel. We replaced the U with u and V with r colours. We note that these colours are not equivalent and therefore the redshift evolution of the colour–mass diagram will be different from the literature. Using the $u - r$ colours, the $M_\star - (u - r)_{rest}$ plane is given by: $(u - r)_{rest} > 0.227 \log_{10} M_\star - 1.16 - 0.352z$, analogous to $U - V$ colours. The colours indicate the red, quiescent/passively evolving galaxies are at the top, in the red sequence region. The green dots indicating the 'green valley' is the transition zone in between. The blue dots indicate the galaxies that reside in the blue star-forming cloud region. Consequently, we can infer from Fig. A1 that the red and blue sequence splitting line analogous to Borch et al. (2006) (see grey solid lines) reside in the blue cloud region. Hence our inability to simply adopt this line to separate blue SFGs from red passively evolving galaxies. For this reason, we use only the Schawinski et al. (2014) criteria (see main text) to separate our sources. We indicate the corresponding percentage of red, green, and blue galaxies for each redshift bin in Fig. A1. The number of red and green galaxies decreases with redshift from *z1* to *z2*. Conversely, the number of blue galaxies increases with redshift from *z1* to *z2*. Our final selection of SFGs combines galaxies residing in the green valley and the blue cloud region in Fig. A1.

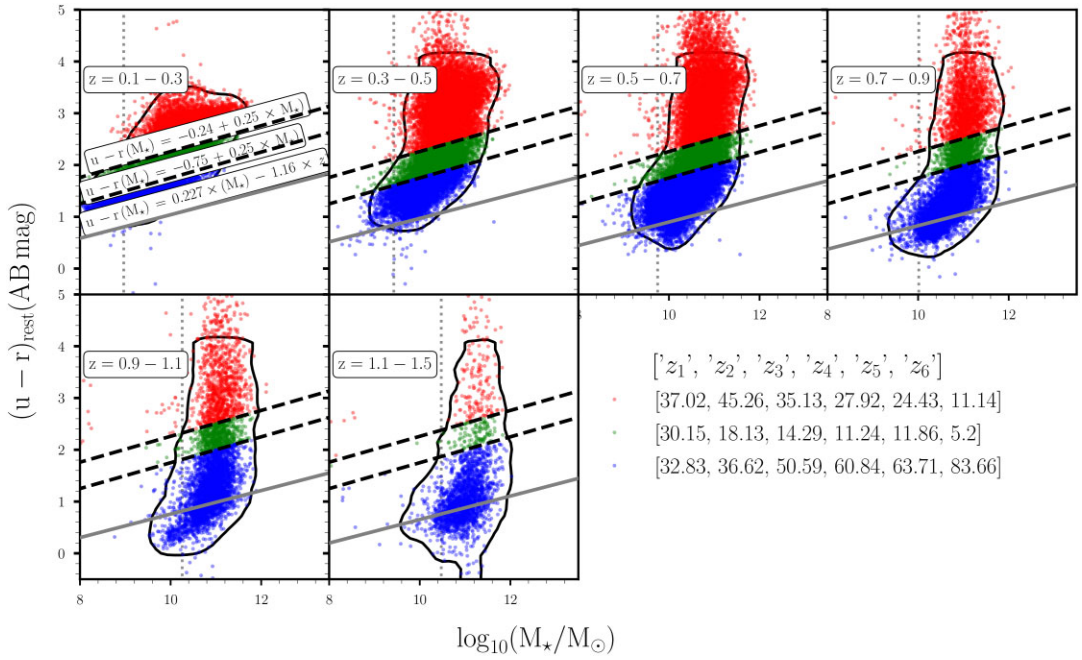

Figure A1. Same as Fig. 3. The colours indicate the red, quiescent/passively evolving galaxies are at the top, in the red sequence with the green dots indicating the 'green valley' is the transition zone in between. We show the red and blue sequence splitting line analogous to Borch et al. (2006) redshift evolution up to $z = 1.5$ as grey solid lines in each panel. The contours enclose those galaxies located in the 90 per cent confidence interval of the data points. The dotted grey vertical lines in each panel represents the mass completeness limit, $M_{\rm lim}$.

Downloaded from https://academic.oup.com/mnras/article/524/4/5229/7227354 by Western Cape University user on 25 April 2024

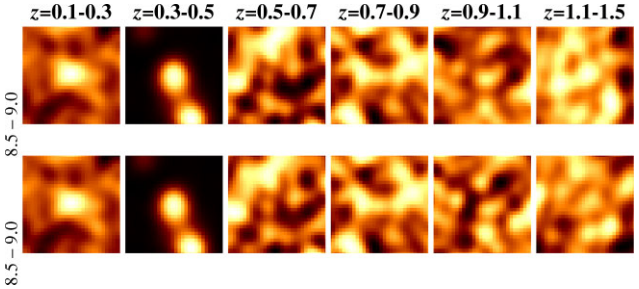

Figure B1. Mean stacked 610 MHz radio images for the same redshift and stellar mass bins for all galaxies (top) and the SFG (bottom) populations, respectively. See Fig. 5 for more details.

APPENDIX B: STACKING ANALYSIS: DETAILS AND TESTS

We discuss some of the issues concerning stacking radio images, including the choice of whether to represent the average as the mean or the median, and in particular, the method to measure total flux. A median stacking analysis is mostly preferable to mean stacking because the median analysis is more stable and robust to small numbers of bright sources. The main problem with a mean stacking analysis is that it is very sensitive to bright outliers, which contaminate on-source flux measurements and introduce considerable noise from nearby, bright neighbours (Lee et al. 2010; Bourne et al. 2012). Many studies that use mean stacking avoid this problem by removing bright sources from all images before stacking. Fig. B1 shows mean stacked 610 MHz radio images for the same redshift and stellar mass bins for the total (top) and the SFG (bottom) populations, respectively. We verify that there is no potential bias in the median stacked fluxes by performing a null test. We draw null stacks (numbers of random sky positions) with equal to the number of sources in each stellar mass and redshift bin. We use the same stacking procedure as when the real sources are used. The results of the null tests fluctuate around zero in for both the total and SFG sources. These random stacks centred around zero indicate that the contribution to our stacked fluxes of

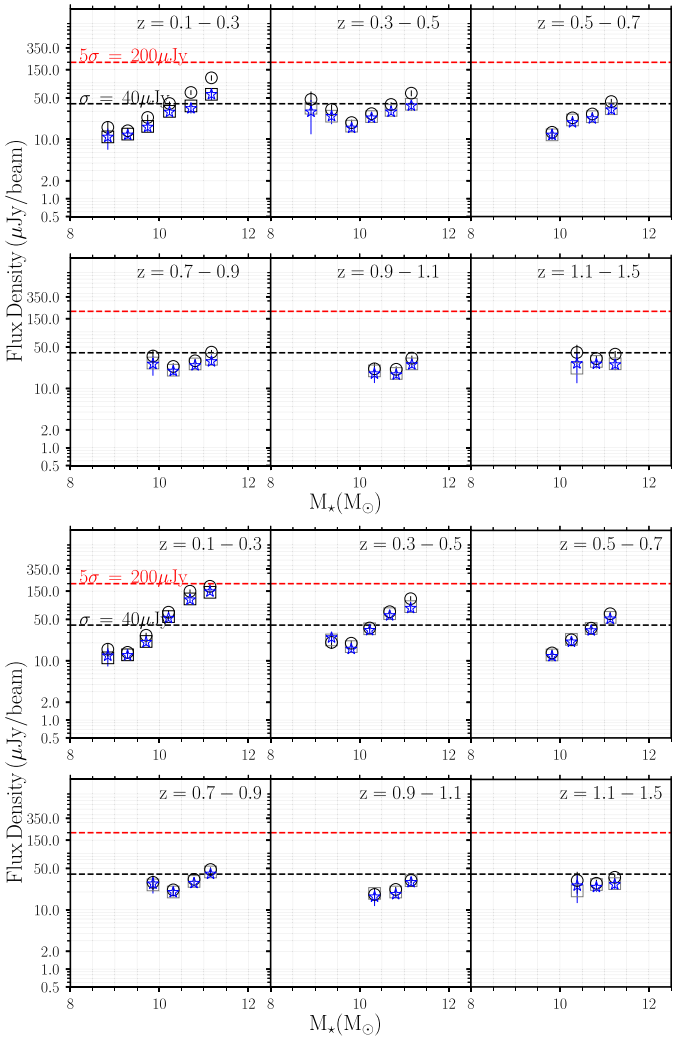

Figure B2. The 610 MHz radio flux density for each source in the redshift and stellar mass bin, measured as in Section 4.1 for all galaxies (top panel) and SFGs (bottom panel) for the median stacked images that show a clear detection. The dashed horizontal lines in each panel represent the σ ($\sim$40 μJy, black) and 5σ ($\sim$200 μJy, red) lines from the original 610 MHz image. The open black circles and open black squares represent the integrated and peak fluxes extracted by PYBDSF. The blue stars represent the corrected flux (i.e. ratio between the integrated flux and the value of the central pixel in the image). The error bars denote the noise level of radio flux density calculated for each image in each redshift and stellar mass bin.

Downloaded from https://academic.oup.com/mnras/article/524/4/5229/7227354 by Western Cape University user on 25 April 2024

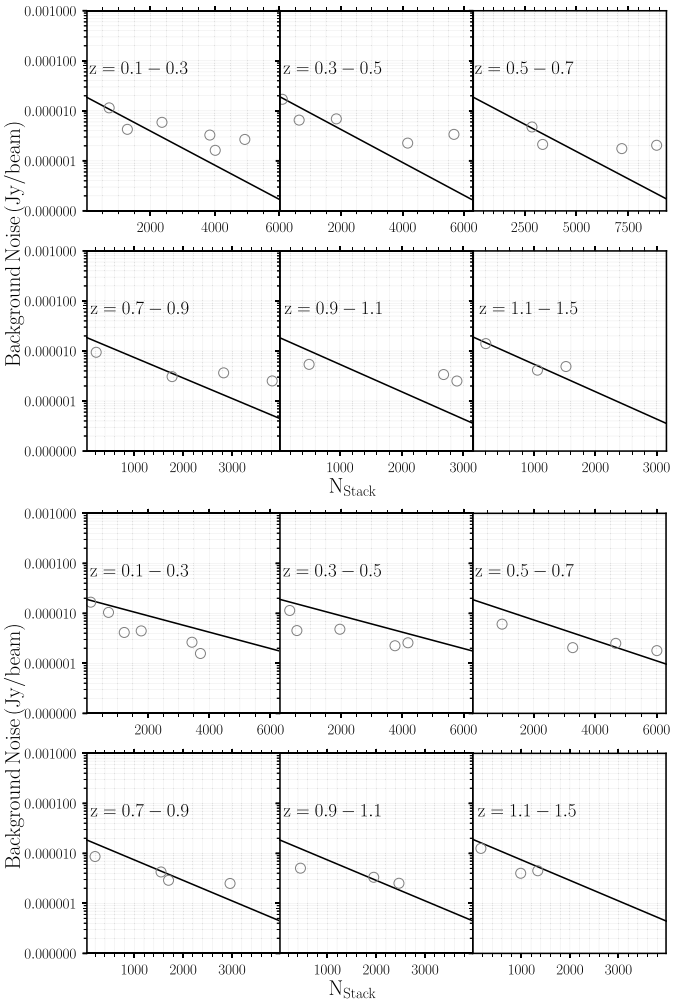

Figure B3. Relationship between the noise in the median stacked images and the number of sources used in the stacked sample ($N_{\rm stack}$) for all galaxies (top panel) and SFGs (bottom panel) for the median stacked images that show a clear detection. The solid black lines are a noise fit of the data where noise $= \sigma/\sqrt{N}$, and $\sigma = \sim 40$ μJy.

source confusion due to the blending of faint sources is negligible (see Stanley et al. 2017; Retana-Montenegro 2022).

The assumption that the pixel value at the position of each catalogue object gives the correct radio flux density for that source is generally good, though it requires a small correction to give the total integrated flux of the source. In general, radio images have pixel units of Janskys (Jy) per beam and do adhere to the convention whereby each pixel value is equal to the flux density of a point source located at that position (see Garn & Alexander 2009; Bourne et al. 2011). The integrated-flux correction is calculated from the stacked 'postage-stamp' image of the total and SFG sample. This image is created by cutting out a 30 pixel square[3] centred on each source and stacking the images by taking the median value of each pixel. The integrated flux is calculated using the PYBDSF source finder (Mohan & Rafferty 2015), and the correction is simply the ratio of this to the value of the central pixel in the image following Bourne et al. (2011).

Ishwara-Chandra et al. (2020) study of the wide-area 610 MHz survey of the ELAIS-N1 field with the GMRT resulted in a flux-limited catalogue in the presence of noise down to ∼200 μJy. They corrected for two important effects, namely Eddington bias (Eddington 1913) and incompleteness, that are key to a sample at faint flux densities. Thus it is not currently known what happens to the number counts and the nature of the sources below ∼200 μJy at 610 MHz. The dashed horizontal lines in each panel of Fig. B2 represents the σ (∼40 μJy, black) and 5σ (∼200 μJy, red) lines from the original 610 MHz image. The comparison to the flux densities extracted from the median stacks showing clear detection of a source at the centre suggests that we probing regimes being strongly affected by confusion (i.e. below rms sensitivity threshold). The open black circles and open black squares represent the integrated and peak fluxes extracted by PyBDSF. The blue stars represent the corrected flux (i.e. ratio between the integrated flux and the value of the central pixel in the image). This correction remains small compared to true variations in stacked fluxes, and essentially all trends remained significant and conclusions unaffected whether or not a bias correction was applied.

In our image stacking implementation, we monitor the decrease of the background noise level. This is comparable to the value expected from the typical GMRT rms of ∼ 40 μJy divided by $\sqrt{N}$ (i.e. a good fit to a $\sigma/\sqrt{\rm N}$ relationship). Fig. B3 indicates that the noise integrated down as expected following Poissonian statistics. We achieve this by measuring the noise in the stacked postage-stamp images around the detected sources (see Dunne et al. 2009; Garn & Alexander 2009).

Downloaded from https://academic.oup.com/mnras/article/524/4/5229/7227354 by Western Cape University user on 25 April 2024

APPENDIX C: OTHER SYSTEMATICS

Studies show that cosmic variance effects are strongest at low redshifts as the effective volume sampled in a redshift bin with $\triangle z = 0.2$ increases with redshift. The large area and relatively decreasing redshift range we consider in this work is necessary to minimize the effect of cosmic variance (see Oogi et al. 2022). We do not account for cosmic variance in our analysis (in line with our previous papers). Driver & Robotham (2010) and Moster et al. (2011) studies provide detailed discussions on cosmic variance in the ELAIS-N1 field.

Cosmic variance is most pronounced at the high-mass end where galaxies are more clustered and at low redshift, where the survey volume is smallest (Muzzin et al. 2013). In Fig. C1, we plot the uncertainty in the abundance of galaxies with $\log_{10}(M_\star/M_\odot) = 11$ due to cosmic variance as a function of redshift. Also plotted in Fig. C1 are the cosmic variance uncertainties from other near-IR surveys such as FIREWORKS (Wuyts et al. 2008), NMBS (Whitaker et al. 2011), and UltraVISTA (McCracken et al. 2012). In Ocran et al. (2021), we estimated that the expected cosmic variance over our relatively large survey area and in our relatively large redshift bins is at the level of 5–10 per cent and thus will not affect our results disproportionately. Over our full redshift range in this study, the uncertainty from cosmic variance as a function of redshift calculated using the prescription of Moster et al. (2011) is ~ 8 per cent $-$ 18 per cent at $\log_{10}(M_\star/M_\odot) = 11$. However, in the interest of simplicity in line with our previous works, we do not consider likely fluctuations from cosmic variance.

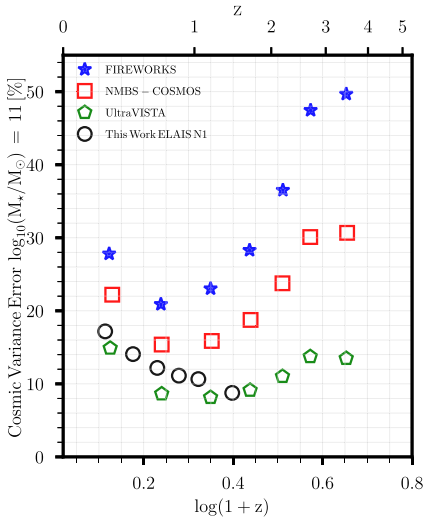

Figure C1. Uncertainty in the number density of galaxies with $\log_{10}(M_\star/M_\odot) = 11$ due to cosmic variance as a function of redshift calculated using the prescription of Moster et al. (2011). The uncertainties in UltraVISTA due to cosmic variance are ~ 8 per cent $-$ 18 per cent at $\log_{10}(M_\star/M_\odot) = 11$ over the full redshift range.

This paper has been typeset from a TEX/LATEX file prepared by the author.

Downloaded from https://academic.oup.com/mnras/article/524/4/5229/7227354 by Western Cape University user on 25 April 2024

© 2023 The Author(s).
Published by Oxford University Press on behalf of Royal Astronomical Society. This is an Open Access article distributed under the terms of the Creative Commons Attribution License (http://creativecommons.org/licenses/by/4.0/), which permits unrestricted reuse, distribution, and reproduction in any medium, provided the original work is properly cited.